Submitted to *EMBO J*

α-Actinin-1 promotes activity of the L-type Ca^{2+} Channel $Ca_V1.2$

Matthew Turner[1$], David E. Anderson[1$], Madeline Nieves-Cintron[2$], Peter Bartels[2$], Andrea M. Coleman[1,2], Peter B. Henderson[2], Kwun Nok Mimi Man[2], Vladimir Yarov-Yarovoy[3], Donald M. Bers[2], Manuel F. Navedo[2], Mary C. Horne[2#], James B. Ames[1#], and Johannes W. Hell[2#]

[1]Department of Chemistry, [2]Department of Pharmacology, and [3]Department of Physiology and Membrane Biology, University of California, Davis, CA 95616, USA.

Running title: *α-Actinin-1 promotes $Ca_V1.2$ gating*
Number of Figures: 7

[$] These authors are equal first authors.
[#] Co-corresponding Authors

Contact information : mhorne@ucdavis.edu ; jbames@ucdavis.edu ; jwhell@ucdavis.edu

Lead contact : jwhell@ucdavis.edu

Keywords : calmodulin, IQ motif structure, open probability, gating charge, surface expression

ABSTRACT

The L-type Ca^{2+} channel $Ca_V1.2$ governs gene expression, cardiac contraction, and neuronal activity. Binding of α-actinin to the IQ motif of $Ca_V1.2$ supports its surface localization and postsynaptic targeting in neurons. We report a bi-functional mechanism that restricts $Ca_V1.2$ activity to its target sites. We solved separate NMR structures of the IQ motif (residues 1646-1664) bound to α-actinin-1 and to apo-calmodulin (apoCaM). The $Ca_V1.2$ K1647A and Y1649A mutations, which impair α-actinin-1 but not apoCaM binding, but not the F1658A and K1662E mutations, which impair apoCaM but not α-actinin-1 binding, decreased single channel open probability, gating charge movement, and its coupling to channel opening. Thus, α-actinin recruits $Ca_V1.2$ to defined surface regions and simultaneously boosts its open probability so that $Ca_V1.2$ is mostly active when appropriately localized.

INTRODUCTION

Ca^{2+} influx through $Ca_V1.2$ is critical for the functions of many organs as strikingly illustrated by Timothy syndrome (Splawski et al., 2004). In this disease a point mutation in $Ca_V1.2$ causes, among other symptoms, lethal arrhythmias, autistic-like behaviors, immune deficiency, and webbing of fingers (Splawski et al., 2004). $Ca_V1.2$ is the main L-type channel in heart (Seisenberger et al., 2000), vascular smooth muscle cells (Ghosh et al., 2017), and brain (Hell et al., 1993, Sinnegger-Brauns et al., 2004). Ca^{2+} influx through $Ca_V1.2$ triggers cardiac contraction, regulates arterial tone (Ghosh et al., 2017), mediates different forms of synaptic long-term potentiation (Grover and Teyler, 1990, Patriarchi et al., 2016, Qian et al., 2017), and controls neuronal excitability (Berkefeld et al., 2006, Marrion and Tavalin, 1998). Furthermore, L-type channels are much more strongly coupled to gene expression than other Ca^{2+} channels

(Cohen et al., 2018, Dolmetsch et al., 2001, Li et al., 2012, Ma et al., 2014). Finally, $Ca_V1.2$ forms a physical and functional complex with the β_2 adrenergic receptor (Davare et al., 2001) making it a prime target for signaling by norepinephrine (Patriarchi et al., 2016, Qian et al., 2017), which is important for wakefulness, attention, and various forms of learning (Berman and Dudai, 2001, Cahill et al., 1994, Carter et al., 2010, Hu et al., 2007, Minzenberg et al., 2008).

$Ca_V1.2$ consists of the pore-forming $\alpha_1 1.2$ subunit and auxiliary $\alpha_2\delta$ and β subunits, which facilitate release from the endoplasmic reticulum and the controlled trafficking of $Ca_V1.2$ to the cell surface (Dai et al., 2009, Dolphin, 2012, 2016, Ghosh et al., 2018, Zamponi et al., 2015). However, $\alpha_2\delta$ and β subunits do not target $Ca_V1.2$ to specific sites in the plasma membrane. Rather, $Ca_V1.2$ anchoring at defined regions at the cell surface is mediated by α-actinin, which binds to the IQ motif in the C-terminus of $\alpha_1 1.2$ (Hall et al., 2013, Tseng et al., 2017).

A systematic yeast two hybrid screen defined three residues in the IQ motif of $\alpha_1 1.2$, whose mutations to alanine residues affect α-actinin binding: K1647A, Y1649A, and I1654A. All three mutations reduced surface expression of $Ca_V1.2$ by ~35% but current density by 70-80% (Tseng et al., 2017). These results suggest that α-actinin binding to the IQ motif promotes not only surface localization but also channel activity. Such a multifunctional role would ensure that $Ca_V1.2$ is mostly active at its ultimate destinations and much less so when in transit and outside its target areas.

The closely related $\alpha_1 1.3$ subunit of the L-type channel $Ca_V1.3$ shares nearly 100 % sequence identity with $\alpha_1 1.2$ in its membrane proximal 165 residues of its C-terminus in which the IQ

motif is embedded (the eponymous Ile is I1654 of $\alpha_1$1.2 and I1609 of $\alpha_1$1.3; Suppl. Fig. 1). Ca^{2+}-free calmodulin (apoCaM) binds to this IQ motif and mutation of I1609 in $\alpha_1$1.3 impairs both, apoCaM binding and open probability Po of $Ca_V1.3$ (Adams et al., 2014, Ben Johny et al., 2013, Ben-Johny et al., 2014). We solved the NMR structures of the third and fourth EF-hands of α-actinin-1 (EF3 and EF4, residues 822-892; Fig. 1A) and of full length apoCaM bound to the α-helical IQ motif of $Ca_V1.2$ (residues 1646-1664). This work provided new insight into the structure of $Ca_V1.2$ especially as relevant for these two critical binding partners and informed experiments that dissected the exact functions of α-actinin versus apoCaM binding. Refined analysis of $Ca_V1.2$ activity by cell attached single channel recording revealed that point mutations that affected α-actinin-1 but not those that affected apoCaM binding dramatically decreased the channel Po by impairing gating charge movement as well as its coupling to channel opening. We conclude that α-actinin plays a dual role by anchoring $Ca_V1.2$ at specific subcellular domains such as the postsynaptic sites and at the same time boosting its open probability. This mechanism ensures that activity of $Ca_V1.2$ is minimal when in transit during secretory trafficking and outside its intended location at the cell surface, where its Ca^{2+} conductance could adversely affect cell functions, but maximal at its final destination.

RESULTS

Binding of α-actinin-1 EF3/EF4 to the $Ca_V1.2$ IQ motif

α-actinin is encoded by four homologous genes with α-actinin-1 and α-actinin-2 being most prominent in neurons (Hall et al., 2013, Hell, 2014, Matt et al., 2018, Wyszynski et al., 1997). α-actinins consist of two N-terminal calponin homology domains (CH1, CH2; residues 19-192), four central spectrin repeats (SR1-4), which form a rod-like coiled-coil structure (Ribeiro Ede et

al., 2014), and four EF hands at their C-termini (residues 750-892; Fig. 1a). We first performed NMR spectroscopy with the CH1/CH2 region (residues 19-192). Two-dimensional NMR spectra of ^{15}N-labeled CH1/CH2 recorded in the presence and absence of unlabeled IQ peptide appeared to be virtually identical, consistent with a lack of IQ binding to CH1/CH2 under NMR conditions (Suppl. Fig. 2a). The lack of IQ binding to the CH1/CH2 domain is supported by absence of detectable binding measured by fluorescence polarization (see below Fig. 1f). In stark contrast, the NMR spectrum of ^{15}N-labeled EF-hand domain of α-actinin-1 (residues 750-892) showed clearly detectable spectral changes upon adding a saturating amount of unlabeled IQ peptide, demonstrating a binding interaction (Suppl. Fig. 2b). The NMR peaks of α-actinin-1 most affected by the binding of IQ (see labeled peaks in Suppl. Fig. 2b) were assigned to residues in EF3 and EF4 (the C-lobe of the EF hand region; residues 822-892). Consistently, the NMR spectrum of ^{15}N-labeled α-actinin-1 EF3/4 (residues 822-892) exhibited large spectral changes upon addition of the IQ peptide (Suppl. Fig. 2c), which are similar to those seen with the construct that contains all four EF-hands (Suppl. Fig. 2b). We conclude that the IQ peptide binds to the α-actinin-1 C lobe.

NMR Structure of α-actinin-1 EF3/4 bound to the IQ motif of Cav1.2

We had previously reported NMR spectral assignments for α-actinin-1 EF3/4 (BMRB accession number 25902) (Turner et al., 2016). We used these assignments to obtain NMR-derived structural restraints for high-resolution structural analysis of α-actinin-1 EF3/4 bound to the Cav1.2 IQ motif (EF3/4-IQ). Atomic-level NMR structures were calculated on the basis of distance restraints derived from analysis of NOESY spectra and long-range orientational restraints derived from residual dipolar coupling (RDC) data (Suppl. Fig. 3a). EF34 in the

116 complex was resolved for 69 residues, starting at T823 and ending at L892. The 10 lowest-
117 energy NMR structures are overlaid in Fig. 1b and structural statistics summarized in Table 1.
118 The overall precision of the ensemble was expressed by an RMSD of 0.3 Å calculated from the
119 coordinates of the main chain atoms. The energy-minimized average structure of EF3/4-IQ (Fig.
120 1c, calculated from the ensembles in Fig. 1b) contained two EF-hand motifs (α1: A826 – A837;
121 α2: M845 – E851; α3: P854 – R863; α4: M880 – Y887; β1: Y842 – T844; β2: A876 – D878)
122 bound to an α-helical IQ motif ($Ca_V1.2$ residues 1646-1664). The NMR structure of EF3/4-IQ
123 (Fig. 1c) was quite similar (1.8 Å RMSD) to the NMR structure of α-actinin-2 bound to the
124 seventh Z-repeat of titin (Atkinson et al., 2001). It contained important intermolecular contacts
125 that stabilize the EF3/4 – IQ interaction (Fig. 1c-e). Most striking were a salt bridge between IQ
126 K1647 and EF3/4 E847/E851 (Fig. 1c) and hydrophobic contacts involving IQ I1654 and EF3
127 F833 (Fig. 1d). The IQ residue F1658 was mostly solvent exposed in the EF3/4-IQ complex
128 contributing minimally if at all to the EF3/4 – IQ interaction (Fig. 1e), in contrast to being buried
129 inside apoCaM in the apoCaM/IQ complex (see below).
130
131 **Validation of the α-actinin-1 EF3/4 - IQ NMR structure by mutagenesis**
132 Mutations in both α-actinin-1 EF3/4 and IQ peptide were designed to verify their predicted
133 intermolecular contacts. A synthetic fluorescein-labeled IQ peptide (residues 1644-1666) was
134 titrated with EF3/4 and fluorescence polarization (FP) monitored to determine their K_d values.
135 The IQ peptide bound to α-actinin-1 EF3/4 with nearly the same affinity as to full-length α-
136 actinin-1 (Fig. 1f; Table 2). The IQ peptide did not bind to α-actinin-1 EF1/2 (Fig. 1f).
137 Accordingly, IQ interacts exclusively with the C-lobe but not N-lobe of the EF hand domain in
138 α-actinin-1.

The salt bridges formed between IQ residue K1647 and α-actinin-1 residues E847 and E851 (Fig. 1c) provided an opportunity for charge inversion experiments. The single residue alterations K1647A and K1647E in the IQ peptide increased the K_d by ~5-fold and mutating E847 and E851 in α-actinin-1 EF3/4 to lysine (K) by ~12-fold (Fig. 1f; Table 2). Combining the E847K/E851K mutations in α-actinin-1 EF3/4 with the K1647E substitution in the IQ peptide mostly but not fully restored the binding affinity to the K1647E IQ peptide. This powerful charge inversion experiment unequivocally identified the importance of those salt bridges for the α-actinin-1 – IQ interaction. Furthermore, I1654 of the IQ motif was predicted to form hydrophobic interactions with F833 in EF3 (Fig. 1d). In fact, the α-actinin-1 EF3/4 mutant F833A showed an ~8-fold decrease in binding affinity, which is consistent with the decrease observed for the I1654A substitution in the IQ peptide (Fig. 1g; Table 2). These results confirmed two important intermolecular interactions that had been seen in the NMR structure (Fig. 1c): a salt bridge contact between K1647 ($Ca_V1.2$) and E847/E851 (α-actinin-1) as well as the linchpin hydrophobic contact between I1654 ($Ca_V1.2$) and F833 (α-actinin-1).

NMR Structure of apoCaM bound to the IQ motif of $Ca_V1.2$.

ApoCaM is predicted to bind to the IQ motif of $Ca_V1.3$ under basal conditions to augment Po (Adams et al., 2014) but no structure has so far been available to aid data interpretation. The ^{1}H-^{15}N HSQC NMR spectrum of ^{15}N-labeled apoCaM showed detectable spectral changes upon adding a saturating amount of unlabeled IQ peptide, demonstrating binding (Suppl. Fig. 2d). The NMR peaks of apoCaM most affected by the binding of IQ (see labeled peaks in Suppl. Fig. 2d) were assigned to residues in its C lobe (CaM EF3/4). Complete NMR spectral assignments for

apoCaM bound to the IQ peptide had been reported previously (Lian et al., 2007). We used these assignments to obtain NMR-derived structural restraints and determine the atomic-level NMR structure of apoCaM bound to the IQ peptide (called apoCaM-IQ). NMR-derived structures were calculated on the basis of NOESY distance restraints and long-range orientational restraints derived from NMR RDC data (Suppl. Fig. 3b) (Tjandra and Bax, 1997). Our NMR chemical shift analysis indicated that the IQ peptide contacted residues in the C-lobe (residues 82-148) but not N-lobe of apoCaM (residues 1-78; Fig. 2). The 10 lowest-energy NMR structures are overlaid in Fig. 2a and structural statistics summarized in Table 3. The overall precision of the ensemble was expressed by an RMSD of 0.6 Å calculated from the coordinates of the main chain atoms. The energy-minimized average structure of apo-CaM/IQ (Fig. 2b, calculated from the ensembles in Fig. 2a) contained two EF-hand motifs (EF3 and EF4) in a semi-open conformation akin to that observed for apoCaM bound to the IQ motif in voltage-gated Na^+ channels (Chagot and Chazin, 2011, Feldkamp et al., 2011). This semi-open apoCaM C-lobe structure was bound to the α-helical IQ motif ($\alpha_1$1.2 residues 1646-1665; Fig. 2b) with an orientation that was opposite to that observed in the crystal structure of Ca^{2+}-CaM bound to IQ (Van Petegem et al., 2005).

The NMR-derived structure of apoCaM bound to $\alpha_1$1.2 IQ peptide contained a number of important intermolecular contacts that stabilized this interaction (Fig. 2b-d). The most striking intermolecular interactions were: (1) a salt bridge between IQ residue K1662 and apoCaM residue E88 (Fig. 2b); (2) hydrophobic contacts involving the side chain atoms of IQ residue I1654 and apoCaM residue F90 (Fig. 2c); and (3) hydrophobic contacts involving the side chain atoms of IQ residue F1658 and apoCaM residues F90/M110 (Fig. 2d).

185

186 **Validation of the apoCaM - IQ NMR structure by mutagenesis**

187 Mutations in both apoCaM and IQ peptide were introduced to verify their predicted
188 intermolecular contacts. We titrated fluorescein-labeled IQ peptide (residues 1644-1666) with
189 apoCaM and measured FP. The Kd for WT IQ peptide was 10 μM (Fig. 2e, Table 4), similar to
190 the Kd of 13 μM in earlier work (Evans et al., 2011). To understand why this Kd is ~20-fold
191 higher than the Kd of 580 nM deducted previously from isothermal titration calorimetry (ITC)
192 measurements (Findeisen et al., 2013), we performed ITC experiments by adding increments of
193 apoCaM (100 μM) to the IQ peptide (10 μM) under near physiological salt concentration (100
194 mM KCl, Suppl. Fig 4a). No heat signal other than that of dilution was detectable (Suppl. Fig.
195 4b). The prior ITC experiments were performed at 5 mM KCl (Findeisen et al., 2013) and may
196 represent a non-physiological electrostatic attraction between oppositely charged apoCaM and
197 IQ that is suppressed by more physiological salt levels (100 mM KCl). Indeed, apoCaM binds to
198 the IQ peptide with nearly 4-fold higher affinity in the absence of salt (Suppl. Fig. 4c; Kd is 2.6
199 μM at 0 KCl and 10 μM at 100 mM KCl).

200

201 According to our FP binding assay, the K1662E mutation in the IQ peptide and the E88K
202 mutation in apoCaM each decreased the binding affinity between IQ peptide apoCaM by more
203 than 5-fold (Fig. 2e; Table 4). Combining the apoCaM E88K mutation with the IQ peptide
204 alteration K1662E restored the binding affinity to some degree although not completely (Fig.
205 2e). The apoCaM mutant F90A showed an ~3.3-fold decrease in binding affinity for WT IQ
206 peptide (Fig. 2f; Table 4). Consistently, I1654A and F1658A substitutions in the IQ peptide
207 resulted in a comparable reduction in their affinity for apoCaM (Fig. 2f). These results confirmed

three important intermolecular interactions seen in the NMR structure: (1) a salt bridge between IQ residue K1662 and apoCaM residue E88; (2) hydrophobic contact between IQ residue I1654 and apoCaM residue F90; and (3) hydrophobic contact between IQ residue F1658 and apoCaM residues F90 and M110.

α-Actinin binding to the $Ca_V1.2$ IQ motif augments open probability of individual channels

Point mutations that impaired α-actinin binding to the IQ motif of $\alpha_1 1.2$ reduced current density upon reconstitution of $Ca_V1.2$ in HEK293 cells by 70-80% but surface expression by only 35-40% as determined by two different methods (Tseng et al., 2017). We performed cell attached recordings to precisely determine single channel parameters of $Ca_V1.2$ as before (Bartels et al., 2018, Davare et al., 2001, Patriarchi et al., 2016, Qian et al., 2017). All three mutations in the IQ motif that impaired α-actinin binding (Table 2) (Tseng et al., 2017), i.e., K1647A, Y1649A, and I1654A, decreased functional availability by 79-93% and overall single channel activity by ~85-92% (Fig. 3a-c; Suppl. Fig. 5, 6a,b; Table 5). Ensemble averages of each experiments were similarly decreased by 84-91% (Fig. 3b,e, Suppl. Fig. 5,6d).

The single channel activity is the product of the number (N) of channels in a patch, the open probability (Po), and unitary current amplitudes (i) of each individual channel (i.e., N·Po·i). Because i was unaffected (Suppl. Fig. 6e) the mutations must affect NPo. Given that surface expression of all three mutations decreased by only 35-40% versus WT $\alpha_1 1.2$ under exactly the same conditions (Tseng et al., 2017), the ~90% reduction of NPo for all three mutants to ~10% of WT $Ca_V1.2$ suggests that Po of the remaining ~60% channels is only ~ 1/6 of the Po of WT $Ca_V1.2$. These observations suggest a remarkable ~6-fold decrease in Po upon loss of α-actinin

binding. To corroborate this notion, we determined N for each recording and derived Po for individual channels. Accordingly, Po is reduced by ~90% for individual channels carrying a K1647A, Y1649A, or I1654A mutation (Fig. 3d; Suppl. Fig. 6c; Table 5). At the same time, the F1658A and K1662E mutations, which diminish apoCaM binding, did not alter NPo.

To further scrutinize the role of α-actinin in Po of $Ca_V1.2$, $Ca_V1.2$ was co-expressed with WT α-actinin-1 or its binding-deficient E847K/E851K mutant. Overexpression of WT but not E847K/E851K mutant α-actinin-1 increased Po of $Ca_V1.2$ WT >2-fold from 3.4% seen with $Ca_V1.2$ alone to 7.9% (Fig. 4a,d; Suppl. Fig. 7c; Table 6). Availability, NPo, and assemble averages were also increased (Fig. 4b,c,e; Suppl. Fig. 7a,b,d; Table 6). Accordingly, in HEK293 cells functional occupancy of $Ca_V1.2$ by endogenous α-actinin appears to be far from complete.

To further test whether α-actinin needs to bind to the $Ca_V1.2$ IQ motif to augment Po, we used a charge inversion experiment by mutating K1647 to the negatively charged glutamyl rather than neutral alanyl residue and then attempted rescue of the expected reduction in Po by pairing expression of K1647E $Ca_V1.2$ with charge inverted E847K/E851K α-actinin-1. Coexpression of K1647E mutant $Ca_V1.2$ with WT α-actinin-1 yielded a low availability, NPo, Po, and ensemble average (Fig. 5; Suppl. Fig. 8; Table 6), which were well below the values observed upon expression of WT $Ca_V1.2$ alone or co-expression of WT $Ca_V1.2$ with E847K/E851K mutant α-actinin-1 (Fig. 4; Table 6). The reduction in availability was statistically significantly, though not fully, rescued when K1647E mutant $Ca_V1.2$ was paired with E847K/E851K mutant rather than WT α-actinin-1 (Fig. 5a; Suppl. Fig. 8a; Table 6). Po also appears to be partially rescued although the p value was 0.07 versus pairing of WT α-actinin-1 with K1647E mutant $Ca_V1.2$.

This rescue of loss of availability and likely of Po for K1647E mutant $Ca_V1.2$ by E847K/E851K mutant α-actinin-1 must be due to either enhanced opening of individual channels, a change in channel surface expression, or both. This rescue is difficult to explain by a mechanism other than that α-actinin-1 binding augments channel activity, including apoCaM binding. Consistently, impairing apoCaM binding to the $Ca_V1.2$ IQ motif by mutating F1658 to Ala or K1662 to Glu had no effect on availability, NPo, Po, and did not affect ensemble averages (Fig. 3; Suppl. Fig. 5, 6).

One possibility for a reduction in Po is that K1647A, Y1649A, and I1654A shift the voltage dependence of $Ca_V1.2$ to more positive potentials such that WT channels open upon depolarization to 0 mV more readily than mutant channels. However, neither the reversal potential nor the voltage dependence of activation was significantly affected by the K1647A and Y1649A mutations and only minimally by the I1654A mutation (Suppl. Fig. 9B,C; Table 7).

To test whether this charge-inversion rescue for the K1647E mutant promoted surface expression of $Ca_V1.2$ we performed surface biotinylation experiments (Fig. 6). As expected, co-expression of WT α-actinin-1 with WT $Ca_V1.2$ increased $\alpha_1$1.2 biotinylation by ~60% versus WT $\alpha_1$1.2 alone. Thus, WT $Ca_V1.2$ expression at the surface is enhanced by α-actinin-1 (Fig. 6a). That the increase in surface expression of WT $Ca_V1.2$ by WT α-actinin-1 overexpression was smaller than the increase in Po is analogous to the smaller effects of the $\alpha_1$1.2 K1647A, Y1649A, and I1654A mutations on surface expression compared to charge density (Tseng et al., 2017) and the larger decrease in Po and NPo we report here (Fig. 3). Importantly, this increase in $Ca_V1.2$ surface expression by α-actinin-1 was lost when WT $\alpha_1$1.2 was co-expressed with

277 E847K/E851K mutant α-actinin-1 or K1647E mutant $\alpha_1$1.2 with WT α-actinin-1 (Fig. 6b).
278 However, the charge inversion we performed by combining these mutants failed to increase
279 surface expression of $Ca_V1.2$ to a degree that would be detectable (Fig. 6b). This result is in
280 contrast to our findings that K1647E $\alpha_1$1.2 availability and likely Po was partially rescued by the
281 E847K/E851K α-actinin-1 charge reversal (Fig. 5). It is conceivable that a small rescue effect
282 did occur but was indiscernible for statistical reasons as 95% confidence intervals (CIs) are
283 larger than a potentially partial rescue of, e.g., 30% of the impairment of ~50% by the K1647E
284 mismatch with WT α-actinin-1 (Suppl. Table 1; a 30% rescue would translate into only an ~15%
285 increase in surface expression).
286
287 **α-Actinin binding to the $Ca_V1.2$ IQ motif augments gating charge movement as well as its**
288 **coupling to channel opening**
289 To test the molecular mechanism underlying the α-actinin-induced increase in Po in more detail
290 we analyzed gating charge movement at the Ba^{2+} current reversal potential (Fig. 7) by whole-cell
291 patch clamp recording. This approach measures all of the Ca^{2+} channels on the surface, thereby
292 ruling out any potential limitation caused by the channel selection inherent in the cell-attached
293 patch recordings in Figs. 3-5. The K1647A, Y1649A, and I1654A mutations reduced gating
294 currents (Q_{on}) by 66-77% (Fig. 7a,b,d; Suppl. Fig. 9a; Table 7) suggesting that α-actinin fosters
295 gating charge movement. This reduction is stronger than the reduction in surface expression
296 (Tseng et al., 2017) but not quite as strong as the 90% reduction in NPo for these mutants (Fig.
297 5). Thus, we investigated whether α-actinin also augments coupling of gating charge movement
298 to channel opening. We analyzed the relationship of tail currents (I_{tail}) to Q_{on} and determined the
299 slopes of the regression curves as an established parameter for quantification of the coupling of

300 Q_{on} to I_{tail} (Tuluc et al., 2009, Yang et al., 2010). Accordingly, the slopes for K1647A, Y1649A,
301 and I1654A mutant $Ca_V1.2$ were strongly reduced compared to WT (Fig. 7c; Table 7). Because
302 large gating events were rare for these mutants, we combined all data from those three mutants
303 for further analysis to better cover that range of the curve. This analysis confirmed that the slope
304 of the resulting curve was substantially smaller than for WT $Ca_V1.2$ (Fig. 7e). Collectively, these
305 data indicate that binding of α-actinin to the $Ca_V1.2$ IQ motif augments not only surface
306 expression but also gating charge movement and its coupling to channel opening. Neither gating
307 charge movements nor their coupling to channel opening were significantly affected by the
308 F1658A or K1662E mutations (Fig. 7; Suppl. Fig. 9a, Table 7), once more arguing against a role
309 in apoCaM binding to the IQ motif in defining NPo under basal conditions.
310
311 **DISCUSSION**
312 The NMR structures of α-actinin-1 and apoCaM bound to the $Ca_V1.2$ IQ motif presented here
313 revealed distinct intermolecular interactions that were verified by mutagenesis experiments
314 involving charge inversion for both interactions. The EF hands in α-actinin-1 are not capable of
315 binding to Ca^{2+} under physiological conditions because their EF-hand loops lack the proper
316 residues for ligating Ca^{2+} with high affinity (Backman, 2015). Therefore, the α-actinin-1 EF-
317 hand domain bound to $Ca_V1.2$ is in the Ca^{2+}-free state under basal conditions ($[Ca^{2+}]_i$ of ~100
318 nM) and adopts a semi-open conformation of Ca^{2+}-free EF-hands like that observed for apoCaM
319 bound to various target proteins (Chagot and Chazin, 2011, Feldkamp et al., 2011, Houdusse et
320 al., 2006). However, the semi-open EF-hand conformation of α-actinin-1 binds to the IQ peptide
321 with a polarity opposite to that of apoCaM (see black arrows in Suppl. Fig. 10a,b). The $Ca_V1.2$
322 residue K1647 at the N-terminal end of the IQ helix forms intermolecular salt bridges with α-

actinin-1 residues E847 and E851. By stark contrast, the IQ helix is rotated 180 degrees upon binding to apoCaM (see black arrows in Suppl. Fig. 10). This opposite orientation places $Ca_V1.2$ residue K1662 at the C-terminal end of the IQ helix in close proximity to CaM residues E85 and E88, which are homologous to α-actinin-1 residues E847 and E851. Similarly, the IQ helices in voltage-gated Na^+ channels bind to apoCaM and Ca^{2+}-saturated CaM with opposite polarity (Hovey et al., 2017). Thus, the orientation of the IQ helix bound to the EF-hand motif may be an important structural determinant of binding specificity and may explain why α-actinin-1 and apoCaM have different functional effects.

Voltage-gated Na^+ channels exhibit Ca^{2+}-dependent inactivation (CDI) mediated by Ca^{2+}-CaM (Ben-Johny et al., 2014, Gabelli et al., 2016), similar to $Ca_V1.2$ (Peterson et al., 1999, Zuhlke et al., 1999). However, the structure of apoCaM bound to the $Ca_V1.2$ IQ motif (Suppl. Fig. 10b) is quite different from previous structures of apoCaM bound to $Na_V1.2$ (Suppl. Fig. 10c) or $Na_V1.5$ (Chagot and Chazin, 2011, Gabelli et al., 2014). The $Na_V1.2$ IQ motif sequence is only 17% identical to that of $Ca_V1.2$ (Suppl. Fig. 10d). $Na_V1.2$ residues A1909, A1915, and Y1919, which are not conserved in $Ca_V1.2$, each make critical contacts with apoCaM. (Suppl. Fig. 10c). The side chain methyl groups of A1909 and A1915 are each 2.5 Å away from the side chain methyl atoms of CaM residues M109 and L85, respectively. The aromatic side chain of Y1919 is in intimate contact with the aromatic side chain of F141 from CaM. Another important difference is that the $Ca_V1.2$ IQ helix binds to apoCaM with opposite directionality compared to the $Na_V1.2$ IQ helix (see black arrows in Suppl. Fig. 10b,c). Hence, the salt bridge that connects $Ca_V1.2$ (K1662) to apoCaM (E88) is not conserved in $Na_V1.2$ or $Na_V1.5$ but the large number of non-conserved intermolecular hydrophobic contacts to $Na_V1.2$ (Suppl. Fig. 10c) caused by the

346 opposite binding orientation of the IQ helix should outweigh any stabilization from the salt
347 bridge in $Ca_V1.2$ and may explain why apoCaM binds to $Na_V1.2$ and $Na_V1.5$ with nanomolar
348 affinity (Hovey et al., 2017) compared to the much weaker micromolar affinity of apoCaM
349 binding to $Ca_V1.2$ (Table 4).
350
351 The relatively high dissociation constant for apoCaM binding to the $\alpha_1$1.2 IQ motif (K_d = 10
352 μM) may be outside the physiological concentration range for apoCaM in neurons. Under basal
353 conditions, the cytosolic apoCaM is kept below 1μM (Wu and Bers, 2007) by proteins that have
354 a high affinity for apoCaM. For instance, in neurons neurogranin (RC3) (Huang et al., 2004,
355 Huang et al., 2000, Ran et al., 2003, Zhong et al., 2011) and GAP-43 (P-57) (Cimler et al., 1985)
356 serve as sinks and reservoirs for apoCaM. In neurons, total concentration of CaM is ~10 μM
357 (Egrie et al., 1977, Zhabotinsky et al., 2006), of neurogranin is 20 μM (Huang et al., 2004,
358 Zhabotinsky et al., 2006), and of GAP-43 is 18 μM (Cimler et al., 1985, Zhabotinsky et al.,
359 2006), and their Kd values for apoCaM are in the range of 1-5 μM (Alexander et al., 1987,
360 Huang et al., 2000, Zhabotinsky et al., 2006), resulting in 0.9 μM free CaM under basal
361 conditions (Zhabotinsky et al., 2006). Therefore, on the basis of the relatively low binding
362 affinity of apoCaM (K_d = 10 μM), the fractional binding of apoCaM to $\alpha_1$1.2 can be estimated to
363 be less than 10% ($Y = \frac{[CaM]}{[CaM]+K_D} < 0.1$) under basal physiological conditions in neurons. Recent
364 work suggests that ectopically expressed WT CaM as well as Ca^{2+} binding-deficient CaM_{1234} is
365 in large excess over endogenous CaM (Iacobucci and Popescu, 2017). As a result, CaM_{1234} may
366 occupy a much larger fraction of $\alpha_1$1.2 than the endogenous WT apoCaM. In this scenario

expression of CaM_{1234} could impair CDI as seen earlier (Peterson et al., 1999) by mechanisms other than displacement of endogenous apoCaM as invoked earlier (Peterson et al., 1999).

Alterations of I1609 in $\alpha_1$1.3 (equivalent to I1654 in $\alpha_1$1.2) impair binding of apoCaM to the closely related $Ca_V1.3$ channel and Po, which was interpreted to mean that apoCaM binding to this IQ motif augments Po (Adams et al., 2014). Here we show that the homologous I1654 in the highly conserved IQ motif of $Ca_V1.2$ is not only critical for apoCaM but also α-actinin binding. Accordingly, mutating I1609 could have decreased NPo by impairing α-actinin rather than apoCaM binding. Indeed, cell attached channel recordings showed an ~90% reduction in Po for all three α-actinin binding - deficient $\alpha_1$1.2 IQ mutants. This effect included K1647, which contacts α-actinin (Fig. 1c) but not apoCaM. Consistently, the K1647A mutation reduced binding of α-actinin (Table 2) but not apoCaM (Table 4). The same is true for the Y1649A mutation. Although Y1649 does not form a direct interaction with α-actinin EF3-EF4, the Y1649A mutation does abrogate α-actinin binding in the yeast two hybrid system (Tseng et al., 2017). We suggest that Y1649 is necessary to stabilize the orientation of L1653 and neighboring I1654, which is required for binding to α-actinin (Suppl. Fig. 11a). Thus, our new data indicate that Po is largely determined by α-actinin and not apoCaM binding. In fact, the F1658A and K1662E mutations, which decreased apoCaM binding (Table 4), did affected neither Po (Fig. 3e) nor Q_{on} (Fig. 7a,b,d) and minimally if at all α-actinin binding (Table 2). In support of these results, others found no effect of CaM on $Ca_V1.2$ plasma membrane targeting in HEK293 cells (Bourdin et al., 2010). This conclusion is further supported by the charge inversion experiments of K1647E mutant $\alpha_1$1.2 and E847K/E851K mutant α-actinin-1 in which impaired functional channel availability and likely impaired Po is partially rescued (Fig. 5). These findings support

the functional relevance of the interaction of the positively charge K1647 in the IQ motif with the negatively charged E847 and E851 of α-actinin-1. That the rescue of the reduction in Po of K1647E mutant $\alpha_1$1.2 by E847K/E851K mutant α-actinin-1 is far from complete can in part be explained by analysis of the E851K rotamers (Suppl. Fig. 11b-d). Most of the E851K rotamers are predicted to clash with side chain and backbone atoms within the α-actinin region at the channel - α-actinin interface based on our structure (Fig. 1c), which will most likely affect the positioning of the EF hand region of α-actinin relative to $\alpha_1$1.2 and thereby the α-actinin - $\alpha_1$1.2 interaction. As a result, binding of E847K/E851K mutant α-actinin-1 to $\alpha_1$1.2 will be decreased as compared to WT α-actinin. In fact, binding affinity is also not fully rescued when the K1647E IQ peptide is titrated with E847K/E851K mutant α-actinin-1 EF3/4 segment (Table 2). A change in the exact structure of the region surrounding the IQ motif in full length $\alpha_1$1.2 could be the reason for further impairment of α-actinin binding furnishing a potential explanation for our finding that functional availability and Po is less effectively rescued by the full charge inversion than the in vitro binding affinity.

Further mechanistic insight is provided by the strong reduction in gating charge movement upon loss of α-actinin binding (Fig. 7). The most striking and very clear finding for Q_{on} is the observation that gating charges for the three α-actinin binding-deficient $\alpha_1$1.2 mutants are so small that they are often barely if at all detectable and amplitudes are difficult to determine. Accordingly, α-actinin binding to the IQ motif promotes the outward movement of the S4 segments, which gives rise to the gating charges, presumably by either lowering energy barriers for this motion or by stabilizing the 'outward' conformation of S4 segments. In addition, α-actinin binding to the IQ motif augments also the coupling between this gating movement and

channel opening. This finding is reminiscent of the effect of $Ca_V1.2$ phosphorylation by PKA on S1700, which upregulates this coupling (Fuller et al., 2010, Fuller et al., 2014). Because of the close proximity of S1700 to the IQ motif it is tempting to speculate that phosphorylation of S1700 and α-actinin binding to the IQ motif intersect to facilitate channel gating, possibly through similar effects on overall conformations of $Ca_V1.2$.

All three α-actinin binding - deficient IQ mutants of $Ca_V1.2$ reduced NPo by ~ 90% when channel density was reduced by only 35-40% as seen by surface labeling (Tseng et al., 2017). To further ascertain that a large portion of the reduction in NPo is due to a reduction in Po and not just N, i.e., not only due to a reduction in surface expression, we determined the 95% confidence intervals (CI) for surface biotinylation, surface labeling with antibodies with subsequent analysis by fluorescence activated cell sorting (Bourdin et al., 2010, Yang et al., 2010), Po, and Q_{on} (Suppl. Tables 1-3). The CIs for surface biotinylation and surface antibody labeling are remarkably similar (e.g., 52-69% and 51-71%, respectively, for the most relevant mutant K1647A, with WT being 100%) and overlap not at all with Q_{on} and Po (26-44% and 6-10%, respectively, for K1647A, with WT again being 100%). Thus, the CIs for the 95% CIs for reductions are ~29-49% for surface stainings, 56-74% for Q_{on}, and 90-94% for Po. Accordingly, it appears extremely unlikely that the reductions in surface expression can fully account for the reductions in Q_{on} and Po for α-actinin – binding-deficient Cav1.2; rather loss of surface localization is only responsible for a fraction of the reductions in Q_{on} and Po. Similarly, the reduction in Q_{on} can most likely only partially account for the reduction in Po, supporting the notion that coupling between the movement of the voltage sensor and the channel gate is impaired in addition to the movement of this sensor.

436

437 If loss of α-actinin binding to the IQ motif would not affect Po of individual channels, then NPo
438 of all α-actinin binding - deficient IQ mutants should be ~60% of wild type $Ca_V1.2$. A 90%
439 decrease in NPo means that 60% of the $Ca_V1.2$ channels that remain on the cell surface upon
440 impairment of α-actinin binding carry only ~10% of the current seen for the wild type $Ca_V1.2$
441 population. These effects translate into a 6-fold reduction in Po of individual $Ca_V1.2$ channels
442 upon loss of α-actinin binding.

443

444 Together with earlier work that showed that α-actinin increases surface localization and
445 postsynaptic accumulation of $Ca_V1.2$ (Hall et al., 2013, Tseng et al., 2017), this new work now
446 demonstrates that α-actinin serves a dual role in regulating $Ca_V1.2$ function. It not only promotes
447 $Ca_V1.2$ surface expression but, remarkably, also exerts a strong positive effect on Po. This
448 mechanism allows $Ca_V1.2$ to be minimally active during secretory trafficking or when it is
449 outside its target regions but to become functionally fully engaged when anchored at proper
450 locations such as postsynaptic sites. Thus, coupling of α-actinin binding to both localization and
451 activity of $Ca_V1.2$ are perfectly fine tuned. This mechanism is so far unique. Whether analogous
452 mechanisms apply to other channels and especially other Ca^{2+} channels, which may require
453 potent mechanisms to prevent inappropriate and potentially harmful Ca^{2+} flux from secretory
454 compartments or at the wrong locations on the cell surface, is now an intriguing premise that will
455 inspire future work.

456

457

458

459 **MATERIALS AND METHODS**

460 **NMR spectroscopy**

461 Xenopus calmodulin was expressed in *E. coli* strain BL21(DE3) grown in LB medium
462 (unlabeled proteins) or M9 media supplemented with $^{15}NH_4Cl$ or $^{15}NH_4Cl/^{13}C$-glucose for
463 single- or double-labeled proteins, respectively. Recombinant CaM was prepared as described
464 previously(Zhang et al., 2012).

465

466 Human α-actinin-1_EF12 (residues 750-812) and α-actinin-1_EF34 (residues 822-893) were
467 each subcloned into pET3b vector and expressed in *E. coli* strain BL21(DE3) grown in LB
468 medium (unlabeled proteins) or M9 media supplemented with $^{15}NH_4Cl$ or $^{15}NH_4Cl/^{13}C$-glucose
469 for single- or double-labeled proteins, respectively. α-actinin-1_EF12 and α-actinin-1_EF34
470 were each purified and prepared as described (Turner et al., 2016).

471

472 Unlabeled $Ca_V1.2$ IQ peptide (residues 1644-1664) was purchased from ChinaPeptides. The
473 peptide was dissolved in d6-DMSO to give a peptide concentration of 7.8 mM. An aliquot of
474 peptide (1.5 equivalents) was added to a dilute solution of α-actinin-1_EF34 or apoCaM (50 μM
475 protein dissolved in 20 mM 2-Amino-2-hydroxymethyl-propane-1,3-diol-d11 (Tris-d_{11}) with 50
476 mM NaCl, 5mM dithiothreitol-d10 (DTT-*d10)* and 95% H_2O/5% D_2O) and incubated at 15^0C for
477 1 hour to ensure complete binding of the peptide. The complex was then concentrated to a final
478 concentration of 500 μM in a final volume of 500 μL for NMR experiments.

479

480

481

Production and use of isotope-labeled peptides using pET-31

We expressed ^{15}N- or $^{15}N/^{13}C$-labeled IQ peptide in *E. coli* as a fusion protein with the ketosteroid isomerase (KSI) using the pET31 plasmid (Kuliopulos et al., 1994) (Novagen/EMD Biosciences). KSI fusion proteins are concentrated in inclusion bodies in *E. coli*, protecting the fused peptide from proteolysis. The fusion protein was purified by affinity chromatography under denaturing conditions via a 6x-His tag at the C-terminus. To release the peptide of interest, the purified fusion is cleaved using cyanogen bromide (CNBr). The CNBr cleaves at methionine residues that were engineered between the KSI and peptide, and between the peptide and 6x-His tag. This cleavage mixture is then rotary evaporated to dryness and resuspended in an appropriate ratio of acetonitrile/water, which solublizes primarily the peptide and not KSI. Finally, the peptide is purified by reverse-phase HPLC.

Two complementary oligonucleotides that code for $Ca_V1.2$ IQ peptide (5'p-TTT TAT GCG ACC TTT CTG ATT CAG GAA TAT TTC CGC AAA TTT AAA AAA CGC AAA ATG; 5'p-TTT GCG TTT TTT AAA TTT GCG AAA ATA TTC CTG AAT CAG AAA GGT CGC ATA AAA CAT) were annealed in 40 mM Tris-HCl , pH 8.0, 10mM $MgCl_2$, 50 mM NaCl by heating to 95° C and then cooling slowly (>2h) to room temperature (RT). The annealed, double-stranded insert was then ligated into AlwNI-digested and dephosphorylated pET31 using T4 DNA Ligase. The 5'-phosphorylation augments ligation and the extra Met codons (underlined) provide compatible sticky ends for the AlwNI-cut plasmid as well as the sites of CNBr cleavage. 2 ul of the ligation mixture were transformed into DH5alpha cells and plasmids from individual ampicillin-resistant colonies sequenced. Successful insertions were obtained, including some multiple insertion. We used one of the single-insertion plasmids for expression in M9 minimal media. *E. coli* was lysed

by sonication. The insoluble material was collected by ultracentrifugation and resuspended in 6M guanidine, insoluble material removed by ultracentrifugation, and the supernatant loaded onto a Ni-NTA column equilibrated with 6M guanidine buffer. After elution with 300 mM imidazole, the purified fractions were pooled and then dialyzed against ultrapure water, causing the fusion protein to precipitate. Precipitate was collected by centrifugation and resuspended in 80% formic acid, transferred to a round-bottom flask and injected with N_2 at ~3 psi. For a 2L scale expression, we used 60 ml of formic acid solution and added 2g of solid CNBr to start the cleavage reaction. After overnight reaction, the flask was roto-evaporated to dryness. The clear peptide film was resuspended in 40% acetonitrile / 60% H_2O and mixed for >1h. After centrifugation to remove any insoluble material, the supernatant was lyophilized, resuspended in H_2O + 0.1% trifluoroacetic acid and run over a C18 reverse phase HPLC column using a gradient of 9-28% acetonitrile. Peak fractions were collected, lyophilized, and analyzed by MALDI-MS to identify the desired peptide product. Dry fractions of peptide were resolublized in DMSO-d6 to a concentration of >5mM.

To measure residual dipolar couplings (RDCs) of α-actinin-1_EF34 or apoCaM bound to IQ peptide, the filamentous bacteriophage Pf1 (Asla Biotech Ltd., Latvia) was used as an orienting medium. Pf1 (12 mg/ml) was added to ^{15}N-labeled α-actinin-1_EF34 or apo CaM bound to unlabeled IQ at pH 7.0, to produce weak alignment of the complex.

Haddock structure determination of α-actinin-1/IQ or apoCaM/IQ

The molecular docking of α-actinin-1 and apoCaM to the Cav1.2 IQ motif (residues 1644 – 1664) was performed using the Haddock d-level 2.2 web server as described (van Zundert et al.,

2016). Residual dipolar couplings, chemical shift perturbation, and mutagenesis data were used as structural restraints. For active restraints or ambiguous interaction restraints (AIR), chemical shift perturbation was used, selecting residues whose chemical shift perturbation falls above the average perturbation.

The initial docking calculation used NMR-derived structures of α-actinin-1 or apoCaM as determined in this study, which were each docked with the helical structure of Cav1.2 IQ peptide (residues 1644-1664) (Van Petegem et al., 2005) as input structures for Haddock. A total of 69 and 42 AIR restraints were used for α-actinin-1 and apoCaM, respectively, based on chemical shift perturbation data and 16 active restraints were used for the IQ peptide from chemical shift perturbation. Unambiguous restraints were introduced to define key intermolecular interactions (IQ K1647 - α-actinin-1_EF34 E847; IQ K1647 - α-actinin-1_EF34 E851; IQ K1662 – CaM E88; IQ I1654 - α-actinin-1_EF3/4 F833 and IQ I1654 – apoCaM F90), which were each verified by mutagenesis (Tables 2 and 4).

Initial docking calculations used AIRs based on chemical shift perturbation data and the top 200 structures were selected for simulated annealing and water refinement. The lowest energy structures were then run again, adding unambiguous restraints based on mutagenesis data. Rigid-body docking, simulated annealing, and water refinement were run using the top 200 structures. RDC restraints assigned to α-actinin-1 and apoCaM were then added using the Sani statement, with tensor values Dr and Da calculated using the program PALES (Zweckstetter, 2008). A total of 74 RDC values were used from residues found in regions of regular secondary structure and as deemed reliable by the PALES calculation.

551

552 **Fluorescence polarization (FP) assays**

553 Fluorescein-labeled peptides (100 nM; ChinaPeptides, Shanghai, China) were titrated with
554 increasing concentrations of either purified α-actinin-1 or CaM in FP buffer (50 mM HEPES, pH
555 7.4, 100 mM KCl, 1 mM $MgCl_2$, 0.05 mM EGTA, 5 mM nitrilotriacetic acid) and FP determined
556 with a Synergy 2 plate reader (BioTek, Winooski, VT) as described (Patriarchi et al., 2016,
557 Tseng et al., 2017, Zhang et al., 2014). FP was calculated as $P = (I_v - g*I_h) / (I_v + g*I_h)$; I_v is
558 vertical and I_h are horizontal fluorescence intensity, respectively and g is the correction factor for
559 fluorescein. To obtain binding curves and K_d values, data were fitted in GraphPad Prism 5 to the
560 equation $Y = B*X / (K_d + X)$; B is maximal FP value that would be reached at saturation as
561 determined by extrapolation of the fitted curve.

562

563 **Isothermal titration calorimetry**

564 ITC experiments were performed using a VP-ITC calorimeter (Micro-Cal) at 27°C and data were
565 acquired and processed with MicroCal software as described previously (Wingard et al., 2005).
566 Samples of apoCaM (injectant) and IQ (titrant) were prepared by exchanging each into buffer
567 containing 50 mM HEPES, pH 7.4, 100 mM NaCl, 0.05 mM EGTA and 1 mM $MgCl_2$. The IQ
568 peptide in the sample cell (10 μM, 1.5 mL) was titrated with apoCaM (100 μM) using 35
569 injections of 10 μl each.

570

571 **Expression of Cav1.2 and α-actinin-1 in HEK293 cells**

572 HEK293T/17 cells were maintained in DMEM-10 [Dulbecco's modified Eagle's medium (Life
573 Technologies) supplemented with 10% fetal bovine serum (FBS, Atlanta Biologicals)] at 37 °C

574 in humidified incubators injected with 5% CO_2 and 95% air (Tseng et al., 2017). For expression
575 of $Ca_V1.2$ HEK293T/17 cells were transfected with rat $\alpha_1 1.2$ (GenBank ID: M67515.1) cDNA
576 subcloned into pECFP-C1 vector (Tseng et al., 2017) encoding an in frame N-terminally fused
577 eCFP tag and an HA tag in the S5-H5 extracellular loop of domain II (Green et al., 2007), which
578 does not affect channel properties (Altier et al., 2002). The point mutations in plasmids encoding
579 single-residue K1647A, K1647E, F1648A, Y1649A, I1654A, F1658A, and K1662E exchanges
580 in $\alpha_1 1.2$ were generated via QuikChange II using the above pECFP-C1 rat $\alpha_1 1.2$ plasmid DNA as
581 template as described (Tseng et al., 2017) and the oligonucleotides described in Suppl. Table 1.
582 For full expression of $Ca_V1.2$ cells were also co-transfected with pGWIH-based plasmids
583 encoding the auxiliary subunits rat β_{2A} (Perez-Reyes et al., 1992) and rabbit $\alpha_2\delta$-1 (Ellis et al.,
584 1988). To assess the contributions of α-actinin-1 on $Ca_V1.2$, cells were transfected with pCMV
585 plasmid DNAs encoding WT (Hall et al., 2013) or mutant α-actinin-1. The K847E/K851EE point
586 mutations in α-actinin-1 were produced via QuikChange II mutagenesis as before (Tseng et al.,
587 2017). The forward primer for making the K851E mutation, which was performed first, was 5'p-
588 CCA TGG ACA AAT TGC GCA GAA AGC TGC CAC CCG ACC AGG and reverse primer
589 5'p-CCT GGT CGG GTG GCA GCT TTC TGC GCA ATT TGT CCA TGG. Forward primer
590 for the K847E mutation was 5'p-GAA CTA CAT TAC CAT GAA CAA ATT GCG CCG CGA
591 GCT GCC ACC C and reverse primer 5'p-GGG TGG CAG CTC GCG GCG CAA TTT GTC
592 CAT GGT AAT GTA GTT C. Transfection of HEK293T/17 cells was accomplished using Ca^{2+}
593 phosphate precipitation (Tseng et al., 2017) for single channel recording and surface labeling or
594 Lipofectamine 2000 for analysis of Q_{on}.
595

Cell Surface Biotinylation Assays. Seven hours after transfection, cells were washed once with 150 mM NaCl, 10 mM $NaHCO_2$, pH 7.4 (PBS) and cultured for another 15-17 hours in fresh medium. 22-24 h after transfection cells were either harvested, monodispersed (>95% viability) and then labeled with EZ-link-sulfo-NHS-LC-biotin (Thermo Fisher Scientific) in solution essentially as described (Tseng et al., 2017) or directly labeled while adhered to the petri dish. In the latter case, adherent cells on the dish were washed twice with ice cold PBS containing 0.5 mM Mg^{2+} and 1 mM Ca^{2+} and incubated on ice with PBS containing 0.4 mg/mL EZ-link-sulfo-NHS-LC-biotin for 15 min. The labeling reaction was quenched by three five min washes with 40 mM glycine in PBS containing 0.5 mM Mg^{2+} and 1 mM Ca^{2+} on ice. Cells were harvested by scraping in PBS and collected by centrifugation. Cell pellets were lysed in ice-cold RIPA buffer (50 mM Tris-HCl, pH 7.4, 150 mM NaCl, 5 mM EGTA, 10 mM EDTA, 1% NP-40, 0.05% SDS, 0.4% DOC, and 10% glycerol) supplemented with a cocktail of protease inhibitors (1µg/mL leupeptin (Merck Millipore), 2µg/mL aprotinin (Merck Millipore), 1 µg/mL pepstatin A (Merck Millipore), and 34 µg/mL phenylmethanesulfonyl fluoride (PMSF; Sigma)). The solubilized material was cleared of insoluble debris by centrifugation at 200,000xg for 30 min at 4ºC. Biotinylated constituents in 600 µg of cell protein lysate were affinity purified by incubation with 30 µL of NeutrAvidin conjugated Sepharose beads (Thermo Fisher Scientific) for 2 h at 4°C. Bead-bound material was collected by centrifugation and washed three times with ice-cold buffer, and immobilized proteins were extracted in SDS sample buffer. Proteins were fractionated by SDS-PAGE in 7.5% acrylamide gels and transferred onto polyvinyldene difluoride (PVDF; BioRad) membranes. PVDF membranes were incubated in blocking buffer (BB) consisting of 150 mM NaCl, 10 mM Tris-Cl, pH 7.4 (TBS) with 0.10% Tween (TBST) and 2% bovine serum albumin (BSA; RPI Corp.) for 1 h at RT before incubation with primary

antibodies in BB for 3 h at RT. $\alpha_1$1.2 was detected by antibodies against the HA tag and, for confirmation, the intracellular loop II/III FP1 epitope (Buonarati et al., 2017) and the CNC2 epitope near the C-terminus of $\alpha_1$1.2 (Buonarati et al., 2017). Probing with antibodies against the cytosolic protein vinculin (Cell Signaling Technologies) and α-tubulin (Santa Cruz Biotechnology) were used to correct for variation in protein content in lysates and as negative control for surface biotinylation. Membranes were washed for 40 min with at least five exchanges of TBST, incubated with horseradish peroxidase-conjugated secondary goat anti-mouse antibodies (HA, α-tubulin; Jackson) or mouse anti-rabbit antibodies (FP1, CNC2, vinculin; Jackson) for 1 h at RT, and washed again with TBST with at least five exchanges for 1.5 h. Immunosignals were detected using the horseradish peroxidase substrates Luminata Classico or Crescendo (Merck Millipore) or Femto (Thermo Fisher Scientific) by X-ray film (Denville Scientific Inc.). Multiple exposures over increasing time periods were taken to ensure that all signals were in the linear range (Davare and Hell, 2003, Hall et al., 2006). Films were scanned and assessed via image J to determine signal intensity for each band. Background signals in individual lanes were subtracted from the band signal before further analysis. To correct differences in immunosignal strengths due to potential differences during immunoblotting and film exposures between experiments, the individual immunosignals for each $\alpha_1$1.2 pull-down sample were divided by the sum of all immunosignals from one blot to obtain the relative signal fraction for each band (Degasperi et al., 2014). The mean of the WT control signals from all experiments was then calculated and all fractional values from all samples (WT and mutants) divided by this value (the WT mean transforms to 1 with this algorithm) (Degasperi et al., 2014). All values were then converted to percent, with the mean of WT control equaling

100%. The data were statistically analyzed applying either a student's T-test (two sample comparison) or ANOVA with Bonferroni's post hoc test as before (Tseng et al., 2017).

Cell-attached Patch Clamp Recording

Cell-attached patch clamp recordings were performed as before (Davare et al., 2001, Patriarchi et al., 2016, Qian et al., 2017) on an Olympus IX70 inverted microscope at room temperature (22ºC). Recordings were obtained with an Axopatch 200B amplifier and data were sampled at 10 kHz with a low-pass filter at 2 kHz (3 dB, four pole Bessel) and digitalized with a Digidata 1440 digitizer. Recording electrodes were fabricated from borosilicate capillary glass (0.86 OD) with a Flaming micropipette puller (Model P-97, Sutter Instruments) and polished (polisher from World Precision Instruments; 3.5 - 6.5 MΩ resistance). The extracellular solution contained (in mM) 145 KCl, 10 NaCl, and 10 HEPES, pH 7.4 (NaOH). The high K^+ concentration was used for optimal control of the transmembrane potential under the patch during depolarizations to 0 mV. The pipette solution contained (in mM) 20 tetraethylammonium chloride (TEA-Cl), 110 $BaCl_2$ (as charge carrier), and 10 HEPES, pH 7.3 (TEA-OH). Cells were depolarized from a holding potential of -80 mV to 0 mV every 5 seconds. Event lists were translated from raw Ba^{2+} currents after leak and capacity transients were digitally subtracted. Data were analyzed based on the half-hight criterium (Sachs et al., 1982) with the single channel software provided by pClamp 10. The number of channels (k) in the patch were estimated based on the observed simultaneous and staged openings) over several minutes at the depolarizing test potential (Bartels et al., 2018, Herzig et al., 2007). The k-value is then determined by the observed maximum current amplitude divided by the unitary current amplitude. Data with more than >3 channels ($k > 3$) in the patch were not considered for statistical analysis in order to prevent overinterpretation of channel open

probability. For statistical analysis single channel parameters were corrected by the channel number as previously (Bartels et al., 2009, Schroder et al., 1998). For a sufficient statistical analysis 50-100 Ba^{2+} current traces were recorded on average for each cell for each experimental condition.

Whole-cell patch-clamp recordings

Whole-cell patch clamp recordings were performed as before (Bartels et al., 2018) on an Olympus IX70 inverted microscope at room temperature (22ºC). Macroscopic Ba^{2+} currents (I_{Ba}) of $Ca_v1.2$ were recorded in external solution containing (in mM) 75 CsCl, 40 TEA-Cl, 20 $BaCl_2$, 1 $MgCl_2$, 10 HEPES and 10 Glucose with a pH adjusted to 7.2 (TEA-OH) and an osmolarity of 300-310 (sucrose). The internal pipette solution contained (in mM) 110 CsCl, 30 TEA-Cl, 1 $MgCl_2$, 4 Mg-ATP, and 10 HEPES, pH 7.2 (CsOH), mOsm 290-300 (sucrose). Pipette resistance was usually between 1.7 -2.5 MΩ. The series resistance and the cell capacitance were taken from an Axopatch 200B Amplifier (Molecular Device) and compensated not more than <40% in order to prevent current oscillation. On-gating currents (Q_{on}) were sampled at 50 kHz and lowpass-filtered at 5 kHz and further quantified through current integration over the first 2-3 ms of the beginning of the test pulse. Cells were clamped at a holding potential of -80 mV and depolarized by a 20 ms test pulse of a serious of activating potentials starting from -60 mV to +80 mV to determine the reversal potential (E_{rev}). Tail currents (I_{tail}) were then measured after repolarization to -50 mV for 10 ms. Recorded data were leak and capacity corrected with an online *P/4* protocol. The liquid junction potential was not considered for correction in the experiment. Data acquisition and analysis was obtained with pClamp 10. Curve fitting was performed by using GraphPad Prism VIII software (San Diego).

Acknowledgements

We thank Dr. Elza Kuzmenkina (University of Cologne, Germany) for providing the coding of the algorithm for calculating Assembly Averages.

This work was supported by NIH grants T32 GM113770 (AMC), T32 GM099608 (PBH), R01 HL098200 (MFN), R01 HL121059 (MFN), R01 EY012347 (JBA), R01MH097887 (JWH), R01 AG017502 (JWH), R01 NS078792 (JWH), and the American Heart Association Predoctoral Fellowship AHA 14PRE19900021 (PBH).

Author Contribution

MT, DEA, MN-C, PB, MFN, MCH, JBA, and JWH designed experiments, MT, DEA, MN-C, PB, AMC, PBH, MFN, and MCH performed experiments, MT, DEA, MN-C, PB, AMC, PBH, VY-Y, DMB, MFN, MCH, JBA, and JWH analyzed data, and MT, DEA, MN-C, PB, VY-Y, DMB, MFN, MCH, JBA, and JWH wrote the manuscript.

Conflict of Interest

All authors declare that they do not have any conflict of interest.

Data Availability

The NMR assignments have been deposited in the BMRB (accession number 25902). The atomic coordinates have been deposited into the Protein Databank (6COA and 6CTB).

Supplemental Material is available in the Online version of this article.

REFERENCES

Adams PJ, Ben-Johny M, Dick IE, Inoue T, Yue DT (2014) Apocalmodulin itself promotes ion channel opening and Ca(2+) regulation. Cell 159: 608-22

Alexander KA, Cimler BM, Meier KE, Storm DR (1987) Regulation of calmodulin binding to P-57. A neurospecific calmodulin binding protein. J Biol Chem 262: 6108-13

Altier C, Dubel SJ, Barrere C, Jarvis SE, Stotz SC, Spaetgens RL, Scott JD, Cornet V, De Waard M, Zamponi GW, Nargeot J, Bourinet E (2002) Trafficking of L-type calcium channels mediated by the postsynaptic scaffolding protein AKAP79. J Biol Chem 277: 33598-603

Atkinson RA, Joseph C, Kelly G, Muskett FW, Frenkiel TA, Nietlispach D, Pastore A (2001) Ca2+-independent binding of an EF-hand domain to a novel motif in the alpha-actinin-titin complex. Nat Struct Biol 8: 853-7

Backman L (2015) Calcium affinity of human alpha-actinin 1. PeerJ 3: e944

Bartels P, Behnke K, Michels G, Groner F, Schneider T, Henry M, Barrett PQ, Kang HW, Lee JH, Wiesen MH, Matthes J, Herzig S (2009) Structural and biophysical determinants of single Ca(V)3.1 and Ca(V)3.2 T-type calcium channel inhibition by N(2)O. Cell Calcium 46: 293-302

Bartels P, Yu D, Huang H, Hu Z, Herzig S, Soong TW (2018) Alternative Splicing at N Terminus and Domain I Modulates CaV1.2 Inactivation and Surface Expression. Biophys J 114: 2095-2106

731 Ben Johny M, Yang PS, Bazzazi H, Yue DT (2013) Dynamic switching of calmodulin
732 interactions underlies Ca2+ regulation of CaV1.3 channels. Nature Commun 4: 1717

733 Ben-Johny M, Yang PS, Niu J, Yang W, Joshi-Mukherjee R, Yue DT (2014) Conservation of
734 Ca(2+)/Calmodulin Regulation across Na and Ca(2+) Channels. Cell 157: 1657-70

735 Berkefeld H, Sailer CA, Bildl W, Rohde V, Thumfart JO, Eble S, Klugbauer N, Reisinger E,
736 Bischofberger J, Oliver D, Knaus HG, Schulte U, Fakler B (2006) BKCa-Cav channel
737 complexes mediate rapid and localized Ca2+-activated K+ signaling. Science 314: 615-20

738 Berman DE, Dudai Y (2001) Memory extinction, learning anew, and learning the new:
739 dissociations in the molecular machinery of learning in cortex. Science 291: 2417-9

740 Bourdin B, Marger F, Wall-Lacelle S, Schneider T, Klein H, Sauve R, Parent L (2010)
741 Molecular determinants of the CaVbeta-induced plasma membrane targeting of the CaV1.2
742 channel. J Biol Chem 285: 22853-63

743 Buonarati OR, Henderson PB, Murphy GG, Horne MC, Hell JW (2017) Proteolytic processing
744 of the L-type Ca 2+ channel alpha 11.2 subunit in neurons. F1000Research 6: 1166

745 Cahill L, Prins B, Weber M, McGaugh JL (1994) Beta-adrenergic activation and memory for
746 emotional events. Nature 371: 702-4

747 Carter ME, Yizhar O, Chikahisa S, Nguyen H, Adamantidis A, Nishino S, Deisseroth K, de
748 Lecea L (2010) Tuning arousal with optogenetic modulation of locus coeruleus neurons. Nature
749 Neurosci 13: 1526-33

750 Chagot B, Chazin WJ (2011) Solution NMR structure of Apo-calmodulin in complex with the IQ
751 motif of human cardiac sodium channel NaV1.5. J Mol Biol 406: 106-19

752 Cimler BM, Andreasen TJ, Andreasen KI, Storm DR (1985) P-57 is a neural specific
753 calmodulin-binding protein. J Biol Chem 260: 10784-8

754 Cohen SM, Suutari B, He X, Wang Y, Sanchez S, Tirko NN, Mandelberg NJ, Mullins C, Zhou
755 G, Wang S, Kats I, Salah A, Tsien RW, Ma H (2018) Calmodulin shuttling mediates cytonuclear
756 signaling to trigger experience-dependent transcription and memory. Nature Commun 9: 2451

757 Dai S, Hall DD, Hell JW (2009) Supramolecular Assemblies and Localized Regulation of
758 Voltage-gated Ion Channels. Physiological Rev 89: 411-452

759 Davare MA, Avdonin V, Hall DD, Peden EM, Burette A, Weinberg RJ, Horne MC, Hoshi T,
760 Hell JW (2001) A beta2 adrenergic receptor signaling complex assembled with the Ca2+ channel
761 Cav1.2. Science 293: 98-101

762 Davare MA, Hell JW (2003) Increased phosphorylation of the neuronal L-type Ca(2+) channel
763 Ca(v)1.2 during aging. Proc Natl Acad Sci USA 100: 16018-23

764 Degasperi A, Birtwistle MR, Volinsky N, Rauch J, Kolch W, Kholodenko BN (2014) Evaluating
765 strategies to normalise biological replicates of Western blot data. PLoS One 9: e87293

766 Dolmetsch RE, Pajvani U, Fife K, Spotts JM, Greenberg ME (2001) Signaling to the nucleus by
767 an L-type calcium channel-calmodulin complex through the MAP kinase pathway. Science 294:
768 333-9

769 Dolphin AC (2012) Calcium channel auxiliary alpha(2)delta and beta subunits: trafficking and
770 one step beyond. Nature Rev Neurosci 13: 542-55

771 Dolphin AC (2016) Voltage-gated calcium channels and their auxiliary subunits: physiology and
772 pathophysiology and pharmacology. J Physiol 594: 5369-90

773 Egrie JC, Campbell JA, Flangas AL, Siegel FL (1977) Regional, cellular and subcellular
774 distribution of calcium-activated cyclic nucleotide phosphodiesterase and calcium-dependent
775 regulator in porcine brain. J Neurochem 28: 1207-13

776 Ellis SB, Williams ME, Ways NR, Brenner R, Sharp AH, Leung AT, Campbell KP, McKenna E,
777 Koch WJ, Hui A, Schwartz A, Harpold MM (1988) Sequence and expression of mRNAs
778 encoding the a_1 and a_2 subunits of the DHP-sensitive calcium channel. Science 241: 1661-1664

779 Evans TI, Hell JW, Shea MA (2011) Thermodynamic linkage between calmodulin domains
780 binding calcium and contiguous sites in the C-terminal tail of Ca(V)1.2. Biophys Chem 159:
781 172-87

782 Feldkamp MD, Yu L, Shea MA (2011) Structural and energetic determinants of apo calmodulin
783 binding to the IQ motif of the Na(V)1.2 voltage-dependent sodium channel. Structure 19: 733-47

784 Findeisen F, Rumpf CH, Minor DL, Jr. (2013) Apo states of calmodulin and CaBP1 control
785 CaV1 voltage-gated calcium channel function through direct competition for the IQ domain. J
786 Mol Biol 425: 3217-34

787 Fuller MD, Emrick MA, Sadilek M, Scheuer T, Catterall WA (2010) Molecular Mechanism of
788 Calcium Channel Regulation in the Fight-or-Flight Response. Sci Signal 3: ra70

789 Fuller MD, Fu Y, Scheuer T, Catterall WA (2014) Differential regulation of CaV1.2 channels by
790 cAMP-dependent protein kinase bound to A-kinase anchoring proteins 15 and 79/150. J Gen
791 Physiol 143: 315-24

792 Gabelli SB, Boto A, Kuhns VH, Bianchet MA, Farinelli F, Aripirala S, Yoder J, Jakoncic J,
793 Tomaselli GF, Amzel LM (2014) Regulation of the NaV1.5 cytoplasmic domain by calmodulin.
794 Nature Commun 5: 5126

795 Gabelli SB, Yoder JB, Tomaselli GF, Amzel LM (2016) Calmodulin and Ca(2+) control of
796 voltage gated Na(+) channels. Channels (Austin) 10: 45-54

797 Ghosh D, Nieves-Cintron M, Tajada S, Brust-Mascher I, Horne MC, Hell JW, Dixon RE,
798 Santana LF, Navedo MF (2018) Dynamic L-type CaV1.2 channel trafficking facilitates CaV1.2
799 clustering and cooperative gating. Biochim Biophys Acta Mol Cell Res 1865: 1341-1355

800 Ghosh D, Syed AU, Prada MP, Nystoriak MA, Santana LF, Nieves-Cintron M, Navedo MF
801 (2017) Calcium Channels in Vascular Smooth Muscle. Adv Pharmacol 78: 49-87

802 Green EM, Barrett CF, Bultynck G, Shamah SM, Dolmetsch RE (2007) The tumor suppressor
803 eIF3e mediates calcium-dependent internalization of the L-type calcium channel CaV1.2.
804 Neuron 55: 615-32

805 Grover LM, Teyler TJ (1990) Two components of long-term potentiation induced by different
806 patterns of afferent activation. Nature 347: 477-9

807 Hall DD, Dai S, Tseng P-Y, Malik ZA, Nguyen M, Matt. L, Schnizler K, Shephard A,
808 Mohapatra D, Tsuruta F, Dolmetsch RE, Christel CJ, Lee A, Burette A, Weinberg RJ, Hell JW
809 (2013) Competition Between α-Actinin and Ca2+-Calmodulin Controls Surface Retention of the
810 L-type Ca2+ Channel CaV1.2. Neuron 78: 483-497

811 Hall DD, Feekes JA, Arachchige Don AS, Shi M, Hamid J, Chen L, Strack S, Zamponi GW,
812 Horne MC, Hell JW (2006) Binding of protein phosphatase 2A to the L-type calcium channel
813 Cav1.2 next to Ser1928, its main PKA site, is critical for Ser1928 dephosphorylation.
814 Biochemistry 45: 3448-59

815 Hell JW (2014) CaMKII: Claiming Center Stage in Postsynaptic Function and Organization.
816 Neuron 81: 249-65

817 Hell JW, Yokoyama CT, Wong ST, Warner C, Snutch TP, Catterall WA (1993) Differential
818 phosphorylation of two size forms of the neuronal class C L-type calcium channel a1 subunit. J
819 Biol Chem 268: 19451-7

820 Herzig S, Khan IF, Grundemann D, Matthes J, Ludwig A, Michels G, Hoppe UC, Chaudhuri D,
821 Schwartz A, Yue DT, Hullin R (2007) Mechanism of Ca(v)1.2 channel modulation by the amino
822 terminus of cardiac beta2-subunits. FASEB J 21: 1527-38

823 Houdusse A, Gaucher JF, Krementsova E, Mui S, Trybus KM, Cohen C (2006) Crystal structure
824 of apo-calmodulin bound to the first two IQ motifs of myosin V reveals essential recognition
825 features. Proc Natl Acad Sci USA 103: 19326-31

826 Hovey L, Fowler CA, Mahling R, Lin Z, Miller MS, Marx DC, Yoder JB, Kim EH, Tefft KM,
827 Waite BC, Feldkamp MD, Yu L, Shea MA (2017) Calcium triggers reversal of calmodulin on
828 nested anti-parallel sites in the IQ motif of the neuronal voltage-dependent sodium channel
829 NaV1.2. Biophys Chem 224: 1-19

830 Hu H, Real E, Takamiya K, Kang MG, Ledoux J, Huganir RL, Malinow R (2007) Emotion
831 Enhances Learning via Norepinephrine Regulation of AMPA-Receptor Trafficking. Cell 131:
832 160-73

833 Huang KP, Huang FL, Jager T, Li J, Reymann KG, Balschun D (2004) Neurogranin/RC3
834 enhances long-term potentiation and learning by promoting calcium-mediated signaling. J
835 Neurosci 24: 10660-9

836 Huang KP, Huang FL, Li J, Schuck P, McPhie P (2000) Calcium-sensitive interaction between
837 calmodulin and modified forms of rat brain neurogranin/RC3. Biochemistry 39: 7291-9

838 Iacobucci GJ, Popescu GK (2017) Resident Calmodulin Primes NMDA Receptors for Ca(2+)-
839 Dependent Inactivation. Biophys J 113: 2236-2248

840 Kuliopulos A, Nelson NP, Yamada M, Walsh CT, Furie B, Furie BC, Roth DA (1994)
841 Localization of the affinity peptide-substrate inactivator site on recombinant vitamin K-
842 dependent carboxylase. J Biol Chem 269: 21364-70

843 Li H, Pink MD, Murphy JG, Stein A, Dell'Acqua ML, Hogan PG (2012) Balanced interactions
844 of calcineurin with AKAP79 regulate Ca2+-calcineurin-NFAT signaling. Nat Struct Mol Biol
845 19: 337-45

846 Lian LY, Myatt D, Kitmitto A (2007) Apo calmodulin binding to the L-type voltage-gated
847 calcium channel Cav1.2 IQ peptide. Biochem Biophys Res Commun 353: 565-70

848 Ma H, Groth RD, Cohen SM, Emery JF, Li B, Hoedt E, Zhang G, Neubert TA, Tsien RW (2014)
849 gammaCaMKII Shuttles Ca(2+)/CaM to the Nucleus to Trigger CREB Phosphorylation and
850 Gene Expression. Cell 159: 281-94

851 Marrion NV, Tavalin ST (1998) Selective activation of Ca^{2+}-activated K^{+} channels by co-
852 localized Ca^{2+}channels in hippocampal neurons. Nature 395: 900-905

853 Matt L, Kim K, Hergarden AC, Patriarchi T, Malik ZA, Park DK, Chowdhury D, Buonarati OR,
854 Henderson PB, Gokcek Sarac C, Zhang Y, Mohapatra D, Horne MC, Ames JB, Hell JW (2018)
855 alpha-Actinin Anchors PSD-95 at Postsynaptic Sites. Neuron 97: 1094-1109 e9

856 Minzenberg MJ, Watrous AJ, Yoon JH, Ursu S, Carter CS (2008) Modafinil shifts human locus
857 coeruleus to low-tonic, high-phasic activity during functional MRI. Science 322: 1700-2

858 Patriarchi T, Qian H, Di Biase V, Malik ZA, Chowdhury D, Price JL, Hammes EA, Buonarati
859 OR, Westenbroek RE, Catterall WA, Hofmann F, Xiang YK, Murphy GG, Chen C-Y, Navedo
860 MF, Hell JW (2016) Phosphorylation of Cav1.2 on S1928 Uncouples the L-type Ca2+ Channel
861 from the β2 Adrenergic Receptor. EMBO J 35: 1330-1345

862 Perez-Reyes E, Castellano A, Kim HS, Bertrand P, Baggstrom E, Lacerda AE, Wei XY,
863 Birnbaumer L (1992) Cloning and expression of a cardiac/brain beta subunit of the L-type
864 calcium channel. J Biol Chem 267: 1792-7

865 Peterson BZ, DeMaria CD, Adelman JP, Yue DT (1999) Calmodulin is the Ca2+ sensor for
866 Ca2+ -dependent inactivation of L- type calcium channels. Neuron 22: 549-58.

867 Pettersen EF, Goddard TD, Huang CC, Couch GS, Greenblatt DM, Meng EC, Ferrin TE (2004)
868 UCSF Chimera--a visualization system for exploratory research and analysis. J Comput Chem
869 25: 1605-12

870 Qian H, Patriarchi T, Price JL, Matt L, Lee B, Nieves-Cintron M, Buonarati OR, Chowdhury D,
871 Nanou E, Nystoriak MA, Catterall WA, Poomvanicha M, Hofmann F, Navedo MF, Hell JW
872 (2017) Phosphorylation of Ser1928 mediates the enhanced activity of the L-type Ca2+ channel
873 Cav1.2 by the beta2-adrenergic receptor in neurons. Sci Signal 10: eaaf9659

874 Ran X, Miao HH, Sheu FS, Yang D (2003) Structural and dynamic characterization of a neuron-
875 specific protein kinase C substrate, neurogranin. Biochemistry 42: 5143-50

876 Ribeiro Ede A, Jr., Pinotsis N, Ghisleni A, Salmazo A, Konarev PV, Kostan J, Sjoblom B,
877 Schreiner C, Polyansky AA, Gkougkoulia EA, Holt MR, Aachmann FL, Zagrovic B, Bordignon
878 E, Pirker KF, Svergun DI, Gautel M, Djinovic-Carugo K (2014) The Structure and Regulation of
879 Human Muscle alpha-Actinin. Cell 159: 1447-60

880 Sachs F, Neil J, Barkakati N (1982) The automated analysis of data from single ionic channels.
881 Pflugers Arch 395: 331-40

882 Schroder F, Handrock R, Beuckelmann DJ, Hirt S, Hullin R, Priebe L, Schwinger RH, Weil J,
883 Herzig S (1998) Increased availability and open probability of single L-type calcium channels
884 from failing compared with nonfailing human ventricle. Circulation 98: 969-76

885 Schwieters CD, Kuszewski JJ, Tjandra N, Clore GM (2003) The Xplor-NIH NMR molecular
886 structure determination package. J Magn Reson 160: 65-73

887 Seisenberger C, Specht V, Welling A, Platzer J, Pfeifer A, Kuhbandner S, Striessnig J,
888 Klugbauer N, Feil R, Hofmann F (2000) Functional embryonic cardiomyocytes after disruption
889 of the L-type alpha1C (Cav1.2) calcium channel gene in the mouse. J Biol Chem 275: 39193-9

Sinnegger-Brauns MJ, Hetzenauer A, Huber IG, Renstrom E, Wietzorrek G, Berjukov S, Cavalli M, Walter D, Koschak A, Waldschutz R, Hering S, Bova S, Rorsman P, Pongs O, Singewald N, Striessnig JJ (2004) Isoform-specific regulation of mood behavior and pancreatic beta cell and cardiovascular function by L-type Ca 2+ channels. J Clin Invest 113: 1430-9

Splawski I, Timothy KW, Sharpe LM, Decher N, Kumar P, Bloise R, Napolitano C, Schwartz PJ, Joseph RM, Condouris K, Tager-Flusberg H, Priori SG, Sanguinetti MC, Keating MT (2004) Ca(V)1.2 calcium channel dysfunction causes a multisystem disorder including arrhythmia and autism. Cell 119: 19-31

Tjandra N, Bax A (1997) Direct measurement of distances and angles in biomolecules by NMR in a dilute liquid crystalline medium. Science 278: 1111-4

Tseng PY, Henderson PB, Hergarden AC, Patriarchi T, Coleman AM, Lillya MW, Montagut-Bordas C, Lee B, Hell JW, Horne MC (2017) alpha-Actinin Promotes Surface Localization and Current Density of the Ca2+ Channel CaV1.2 by Binding to the IQ Region of the alpha1 Subunit. Biochemistry 56: 3669-3681

Tuluc P, Molenda N, Schlick B, Obermair GJ, Flucher BE, Jurkat-Rott K (2009) A CaV1.1 Ca2+ channel splice variant with high conductance and voltage-sensitivity alters EC coupling in developing skeletal muscle. Biophys J 96: 35-44

Turner M, Anderson DE, Rajan S, Hell JW, Ames JB (2016) Chemical shift assignments of the C-terminal EF-hand domain of alpha-actinin-1. Biomol NMR Assign 10: 219-22

Van Petegem F, Chatelain FC, Minor DL, Jr. (2005) Insights into voltage-gated calcium channel regulation from the structure of the CaV1.2 IQ domain-Ca2+/calmodulin complex. Nat Struct Mol Biol 12: 1108-15

van Zundert GC, Rodrigues JP, Trellet M, Schmitz C, Kastritis PL, Karaca E, Melquiond AS, van Dijk M, de Vries SJ, Bonvin AM (2016) The HADDOCK2.2 Web Server: User-Friendly Integrative Modeling of Biomolecular Complexes. J Mol Biol 428: 720-5

Wingard JN, Chan J, Bosanac I, Haeseleer F, Palczewski K, Ikura M, Ames JB (2005) Structural analysis of Mg2+ and Ca2+ binding to CaBP1, a neuron-specific regulator of calcium channels. J Biol Chem 280: 37461-70

Wu X, Bers DM (2007) Free and bound intracellular calmodulin measurements in cardiac myocytes. Cell Calcium 41: 353-64

Wyszynski M, Lin J, Rao A, Nigh E, Beggs AH, Craig AM, Sheng M (1997) Competitive binding of a-actinin and calmodulin to the NMDA receptor. Nature 385: 439-442

Yang T, Xu X, Kernan T, Wu V, Colecraft HM (2010) Rem, a member of the RGK GTPases, inhibits recombinant CaV1.2 channels using multiple mechanisms that require distinct conformations of the GTPase. J Physiol 588: 1665-81

Zamponi GW, Striessnig J, Koschak A, Dolphin AC (2015) The Physiology, Pathology, and Pharmacology of Voltage-Gated Calcium Channels and Their Future Therapeutic Potential. Pharmacol Rev 67: 821-70

Zhabotinsky AM, Camp RN, Epstein IR, Lisman JE (2006) Role of the neurogranin concentrated in spines in the induction of long-term potentiation. J Neurosci 26: 7337-47

930 Zhang Y, Li Z, Sacks DB, Ames JB (2012) Structural basis for Ca2+-induced activation and
931 dimerization of estrogen receptor alpha by calmodulin. J Biol Chem 287: 9336-44

932 Zhang Y, Matt L, Patriarchi T, Malik ZA, Chowdhury D, Park DK, Renieri A, Ames JB, Hell
933 JW (2014) Capping of the N-terminus of PSD-95 by calmodulin triggers its postsynaptic release.
934 EMBO J 33: 1341-1353

935 Zhong L, Kaleka KS, Gerges NZ (2011) Neurogranin phosphorylation fine-tunes long-term
936 potentiation. Eur J Neurosci 33: 244-50

937 Zuhlke RD, Pitt GS, Deisseroth K, Tsien RW, Reuter H (1999) Calmodulin supports both
938 inactivation and facilitation of L-type calcium channels. Nature 399: 159-62

939 Zweckstetter M (2008) NMR: prediction of molecular alignment from structure using the
940 PALES software. Nat Protoc 3: 679-90

941

942 **Table 1: NMR Structural Statistics for α-actinin-1 EF34/IQ**

943

NMR Structural Restraints	
Intermolecular NOEs	73
Hydrogen Bonds	62
RDC Q-Factor	0.095
$^{1}D_{HN}$RDC	34
RDC Correlation Coefficient (R)	0.99
Root mean squared deviation from average structure	
α-actinin-1 backbone atoms	0.5 Å ± 0.3 for 200 structures
α-actinin-1 backbone atoms (refined)	0.3 Å ± 0.2 for 50 structures
Haddock Scoring	
Cluster Size	194
Van der Waals Energy	-40.2 ± 6.2
Electrostatic Energy	-395.4 ± 37.1
Restraints Violation Energy	278.0 ± 6.23
Ramachandran Plot	
Most Favored Regions	96.7 %
Allowed Regions	2.2 %
Unfavored Regions	1.1 %

944

945 **Table 2: Kd (in μM) for α-actinin-1 EF3/EF4 binding to IQ as determined by FP.**
946 Shown are mean+SD (n=3 for all conditions)
947

		α-actinin-1 EF3/4			
		WT	**E847K/E851K**	**F833A**	
$Ca_V1.2$ IQ	**WT**	14 ± 2	167 ± 20	100 ± 10	
	K1647E	73 ± 10	27 ± 2	/	
	K1647A	67 ± 10	/	/	
	Y1649A	42 ± 4	/	/	
	I1654A	200 ± 20	/	/	
	F1658A	20 ± 2	/	/	
	K1662E	20 ± 2	150 ± 20	/	

948

949 **Table 3: NMR Structural Statistics for apo CaM/IQ**
950

NMR Structural Restraints	
Hydrogen Bonds	62
RDC Q-Factor	0.089
$^{1}D_{HN}$RDC	36
RDC Correlation Coefficient (R)	0.99
Root mean squared deviation from average structure	
CaM backbone atoms	0.6 Å ± 0.3 for 200 structures
CaM backbone atoms (refined)	0.6 Å ± 0.2 for 92 structures
Haddock Scoring	
Cluster Size	200
Van der Waals Energy	-56.8 ± 0.6
Electrostatic Energy	-463.5 ± 20.7
Restraints Violation Energy	99.8 ± 36.2
Ramachandran Plot	
Most Favored Regions	89.8 %
Allowed Regions	8.0 %
Unfavored Regions	2.3 %

951
952

953 **Table 4: Kd (in μM; means±SEM) for apoCaM binding to IQ as determined by FP.**
954 Shown are mean+SD (n=3 for all conditions)
955

		apoCaM			
		WT	**E88K**	**F90A**	
$Ca_V1.2$ IQ	**WT**	10 ± 3	50 ± 10	33 ± 5	
	K1647E	12 ± 3	53 ±1 0	/	
	K1647A	11 ± 3	/	/	
	Y1649A	16 ± 4	/	/	
	I1654A	68 ±1 0	/	/	
	F1658A	33 ± 5	/	/	
	K1662E	60 ± 10	26 ± 5	/	

956

Table 5: Biophysical properties of $Ca_V1.2$ microscopic single channel currents for WT versus IQ motif mutants

Gating parameter	*Availability (%)*	*NP_{open} (%)*	*P_{open} (%)*	*I(mean ensemble avg.) [fA]*	*unitary current (pA)*	*sweeps*	*n*
WT [a]	56.2±6.3	3.6±0.75	3.4±0.7	14.8±3.1	0.89±0.02	2744	32-35
K1647A [b]	21.0±7.6**	0.30±0.09***	0.27±0.08***	2.3±0.6**	0.97±0.05	868	12
F1648A [c]	69.7±6.6	3.2±0.7	3.2±0.7	14.4±2.6	0.87±0.02	1221	13-14
Y1649A [d]	16.8±6.8**	0.53±0.17**	0.49±0.2***	1.9±0.5**	0.84±0.06	556	8
I1654A [e]	7.0±2.1**	0.44±0.2***	0.35±0.2***	1.4±0.6***	0.94±0.04	589	7
F1658A [f]	47.8±7.6	5.0±2.2	4.7±2.2	18.8±8.6	0.90±0.03	986	12
K1662E [g]	62.5±9.7	4.2±1.1	4.1±1.1	15.9±4.2	0.99±0.03	1015	13
One-Way ANOVA	a-b† a-d† a-e†	a-b‡ a-d‡ a-e‡	a-b‡ a-d‡ a-e‡	a-b‡ a-d‡ a-e‡	NS		

HEK293 cells were transiently transfected with WT and IQ domain mutant $Ca_V1.2$ ($\alpha_1$1.2, $\alpha_{2\text{-}}\delta_1$ and β_{2a}) for recording of single channel activity in 110 mM Ba^{2+} upon depolarized from a holding potential -80 mV to a test potential (TP) of 0 mV for 2 seconds at an interpulse rate of 0.14 Hz. Availability is quantified as the fraction of sweeps showing channel activity over the number of total sweeps. Statistical significance was determined by pairwise multiple testing among groups against the WT[a] by a One-way ANOVA with Bonferroni† post-hoc test or Welch ANOVA with Tamhane‡ T2 test. Given are mean values ± SEM (*p < 0.05, **p < 0.01, ***p < 0.0001).

968
969 **Table 6**: **Effect of α-actinin-1 ectopic expression on biophysical properties of $Ca_V1.2$**
970 **single channel currents**

Gating parameter	Availability (%)	NP_{open} (%)	P_{open} (%)	I(Mean ensemble Avg.) [fA]	unitary current (pA)	sweeps	n
WT [a]	56.6±6.3	3.6±0.75	3.4±0.69	14.8±3.1	0.89±0.02	2744	32-35
WT+ α-Actinin [b]	76.5±6.2*	9.2±2.0**	7.9±2.0*	31.3±7.5*	0.84±0.02	2388	23-25
WT+ EE847/851KK [c]	32.9±7.5***	1.9±0.7**	1.8±0.7*	7.4±2.8*	0.83±0.03	1252	13
F1647E+ α-Actinin [d]	43±5.0	1.8±0.3	1.7±0.3	8.5±1.5	0.83±0.01	2601	30
F1647E+ EE847/851KK [e]	67.9±6.9**	2.6±0.5	2.5±0.5	11.3 ±2.7	0.84±0.02	1376	16
unpaired T-test	a-b¥ b-c¥ d-e¥	a-b¥ b-c¥	a-b¥ b-c¥ d-e p=0.7	a-b¥ b-c¥ d-e p=0.7	NS		

971
972 HEK293 cells were transiently transfected with WT $Ca_V1.2$ ($\alpha_1$1.2, α_2-δ_1 and β_{2a}) and, if indicated,
973 with α-Actinin-1 WT or E847K/E851K. Single channel activity was obtained as in Table 5.
974 Statistical significance was determined by pairwise testing of $Ca_V1.2$ WT alone vs. $Ca_V1.2$ WT +
975 α-Actinin WT, $Ca_V1.2$ WT + α-Actinin-1 WT vs. $Ca_V1.2$ + α-Actinin-1 E847K/E851K, and $Ca_V1.2$
976 K1647E + α-Actinin-1 WT vs. $Ca_V1.2$ K1647E + α-Actinin-1 E847K/E851K with an unpaired T-
977 test¥. Given are mean values ± SEM (*p < 0.05, **p < 0.01, ***p < 0.0001). Values for $Ca_V1.2$ WT
978 are provided in grey tone for comparison from Table 5.
979

Table 7. Biophysical properties of $Ca_V1.2$ macroscopic whole cell patch currents for WT versus IQ motif mutants

Analysis	I-V			G-V			Charge movement	I_{Tail}/Q_{on}
Para–meter	$V_{1/2act.}$ (mV)	$k_{act.}$	$E_{rev.}$ (mV)	$V_{1/2act.}$ (mV)	k_{low}	k_{high}	Qon (fC/pF)	slope
WT[a]	-18.5±0.5	-4.2±0.4 (10)	51.3±1.3	-6.5.0±0.4	7.0±0.3 (16)	-8.5±27.4	3.8±0.9 (18)	3.9±1.5 (16)
K1647A[b]	-19.9±0.9	-5.9±0.6 (11)	55.2±2.0	-8.5.0±0.9	8.5±0.8 (15)	9.0±10.5	1.3±0.3* (15)	0.26±1.5 (15)
Y1649A[c]	-19.9±0.6	-4.0±0.5 (10)	49.2±1.5	-6.3.0±0.7	7.5±0.8 (16)	28.7±6.9	0.98±0.3** (13)	0.19±1.0 (12)
I1654A[d]	-12.6±1.0****	-5.4±0.7 (5)	48.2±2.6	-2.5±0.9**	7.5±0.9 (13)	38.5±11.5	0.87±0.3** (13)	1.3±0.6 (12)
F1658A[e]	-26.5±1.1**	-4.5±0.9 (6)	58.6±4.1	-10.6±1.4**	5.3±1.6 (11)	20.2±3.9	2.8±0.6 (13)	3.1±1.4 (12)
K1662E[f]	-20.2±0.4	-4.2±0.3 (12)	50.1±1.2	-6.1.0±0.7	7.9±0.8 (21)	49.2±19.4	3.5±1.1 (17)	2.2±1.0 (14)
ANOVA/ T-Test	a-d† a-e†	NS	NS	a-d† a-e†	NS	NS	a-b† a-c† a-d†	

HEK293 cells were transiently transfected with WT $Ca_V1.2$ ($\alpha_1$1.2, α_{2}-δ_1 and β_{2a}). Whole cell patch recording was performed in 20 mM Ba^{2+} (see Fig. 7).To obtain current - voltage relationships (I-V), currents were recorded upon depolarization from a holding potential of -80 mV to increasingly more positive potentials (see Figure 7A for details). The voltage for half maximal activation ($V_{1/2act}$), activation constant (k_{act}), and reversal potential (E_{rev}) was determined. To obtain conductance - voltage relationships (G-V), tail currents (I_{Tail}) were recorded upon repolarization to -50 mV following depolarization from a holding potential of -80 mV to increasingly more positive potentials (see Figure 7A for details). The activation kinetics for G-V were best described by double exponential fits and the rate constants k_{high} and k_{low} were determined accordingly. Total charge movement (Q_{on}) and the ratio of I_{Tail} / Q_{on} were determined as in Fig. 7. Statistical significance was determined by pairwise multiple testing among groups against the WT[a] by a One-way ANOVA with a Bonferroni† post-hoc test. Given are mean values ± SEM (*p < 0.05, **p < 0.01, ****p < 0.0001).

Supplemental Tables 1-3

Supplemental Table 1. 95% Confidence intervals (CI) for surface labelling, Qon, and Po for WT and IQ mutant $Ca_V1.2$

Given are means±SEM and 95% CIs for experimental values. The number of experiments is shown in parenthesis. *The biotinylation and flow cytometry data are based on data originally published by Tseng et al (2017).

Parameter	*Biotin-ylation (% of WT)	95% CI	*Flow Cytometry (% of WT)	95% CI	Gating Current Qon (% of WT)	95% CI	P_{open} (% of WT)	95% CI
$\alpha_1$1.2 WT	100±0 (16)	0-0	100±0 (7)	0-0	100±24 (18)	78-122	100±20 (35)	87-113
K1647A	61±5 (11)	52-69	61±7 (7)	51-71	35±9 (15)	26-44	8±2 (12)	6-10
F1648A	94±7 (8)	85-104	ND		ND		93±20 (14)	73-114
Y1649A	66±5 (12)	61-72	63±7 (6)	52 - 74	26±8 (13)	18-35	15±5 (8)	8-22
I1654A	68±4 (10)	63-73	61±8 (6)	49-74	23±10 (13)	1 -34	10±5 (7)	3-17
Q1655A	85±5 (7)	78-92	104±6 (4)	93-116	ND		ND	
F1658A	ND		ND		76±16 (13)	59-93	139±64 (12)	45-121
K1662E	ND		ND		93±29 (17)	52-134	120±32 (13)	86-154

Supplemental Table 2. 95% Confidence intervals (CI) for surface biotinylation for $Ca_V1.2$ / α-actinin-1 charge inversion experiments

Given are means±SEM and 95% CIs (based on original data from this manuscript). The number of experiments is shown in parenthesis.

Parameter	Biotinylation (%)	95% CI
$\alpha_1$1.2 WT	100±6 (7)	86-114
$\alpha_1$1.2 WT + α-Actinin WT	153±6 (7)	139-167
$\alpha_1$1.2WT+ α-Actinin WT	100±9 (5)	74-126
$\alpha_1$1.2 WT + α-Actinin EE/KK	48±9 (5)	24-72
$\alpha_1$1.2 K1647E + α-Actinin WT	60±5 (5)	47-73
$\alpha_1$1.2 K1647E + α-Actinin EE/KK	55±5 (4)	39-71

Supplemental Table 3. 95% Confidence intervals (CI) for Po for $Ca_V1.2$ / α-actinin-1 charge inversion experiments

Given are means±SEM and 95% CIs (based on original data from this manuscript). The number of experiments is shown in parenthesis.

Parameter	P_{open} (%)	95% CI
$\alpha_1$1.2 WT	100±20 (35)	87-113
$\alpha_1$1.2 WT + α-Actinin WT	233±59 (23)	186 - 280
$\alpha_1$1.2 WT+ α-Actinin EE/KK	55±22 (13)	32-78
$\alpha_1$1.2 K1647E + α-Actinin WT	100±18 (30)	87-113
$\alpha_1$1.2K1647E + α-Actinin EE/KK	147±28 (16)	120-174

Fig. 1 | α-Actinin-1 makes electrostatic and hydrophobic contacts with Cav1.2.

a, Linear model of α-actinin domains (CH, calponin homology domains; SR, spectrin repeats; EF, EF hands). Bars and numbers on top of the model depict the segments used in this work.

b, Ensemble of 10 lowest energy NMR-derived structures of α-actinin-1_EF34 (cyan) bound to IQ peptide (red). Structural statistics are given in Table 1.

c, Energy minimized average structure of α-actinin-1_EF34 (cyan) bound to IQ (red), revealing intermolecular salt bridges between K1647 of IQ and E847/E851 of α-actinin-1. The K1647 side chain amino nitrogen atom is 2.8 Å and 2.5 Å away from the side chain carbonyl oxygen atoms of E847 and E851, respectively.

d, Intermolecular hydrophobic contacts between I1654 of IQ (red) and F833 of α-actinin-1 (cyan). The I1654 side chain methyl carbon atom is 2.9 Å away from the closest aromatic ring atom of F833. Side-chain atoms are colored yellow.

e, Lack of direct contacts between F1658 of IQ (red) and α-actinin-1 (cyan). The aromatic side chain of F1658 is primarily solvent exposed and does not directly contact α-actinin-1. The aromatic ring of F1658 is closest to the aromatic ring of Y859 and β-methylene carbon of Q856 of α-actinin-1, which are 5.2 Å and 4.3 Å apart, respectively.

f, FP titrations show binding of WT α-actinin-1_EF34 to IQ peptides WT (black) and K1647E (red), of α-actinin-1_EF34 mutant E847K/E851K to IQ peptides WT (green) and K1647E (purple), of full-length α-actinin-1 to IQ WT (o), and lack of IQ binding to α-actinin-1_CH1-CH2 (+) and α-actinin-1_EF12 (x; see Table 2 for binding parameters and standard errors).

g, FP titrations showing binding of wild type α-actinin-1_EF34 to IQ peptides WT (black) and I1654A (purple) and of ACTN1_EF34 mutant F833 to IQ WT (red; see Table 2 for binding parameters and standard errors).

Fig. 2 | ApoCaM makes electrostatic and hydrophobic contacts with Cav1.2.

a, Ensemble of 10 lowest energy NMR-derived structures of apo CaM/IQ complex. Structural statistics are given in Table 3.

b, Energy minimized average structure of apoCaM (cyan) bound to IQ (red), showing an intermolecular salt bridge between IQ K1662 and apoCaM E88. The K1662 side chain amino nitrogen atom is 2.7 Å away from the side chain carbonyl oxygen of E88.

c, Intermolecular hydrophobic contacts between IQ I1654 (red) and apoCaM F90 (cyan). Side chain atoms colored yellow. The I1654 side chain methyl carbon atom is 2.2 Å away from the closest aromatic ring atom of F90.

d, Intermolecular hydrophobic contacts between F1658 of IQ and F90/M110 in apoCaM. The aromatic side chain atoms of F1658 are 2.3Å and 2.6 Å away from the closest side chain atom of F90 and M110, respectively.

e, FP titrations showing binding of apoCaM to IQ peptides WT (black) and K1662E (red) and of apoCaM mutant E88K to IQ WT (green) and IQ peptide K1662E (purple, “charge inversion”; see Table 4 for binding parameters and standard errors).

f, FP titrations showing binding of apo-CaM to IQ peptides WT (black), I1654A (red), and F1658A (green) and of apoCaM mutant F90A to IQ WT (blue; see Table 4 for binding parameters and standard errors).

Fig. 3 | $Ca_V1.2$ mutations that affect α-Actinin-1 drastically decrease channel open probability.

HEK293 cells were transfected with $\alpha_1$1.2, $\alpha_2\delta$-1, and β_{2A} and cultured for 22-24h before cell attached patch recording in 110 mM Ba^{2+}.

a, Single $Ca_V1.2$ channel recordings of $Ca_V1.2$ WT and K1647A. Holding potential (HP) was -80 mV and test potential (TP) 0 mV. Shown are 20 consecutive sweeps from representative experiments.

b, Mean assembly averages for all experiments with $Ca_V1.2$ WT and K1647A, which are based on a total of 2744 and 868 sweeps, respectively (see Table 5).

c-e, Means ± SEM for availability (i.e., likelihood that a sweep had at least one event; c), Po (d), and the mean of the current of a single channel at any point in time calculated from the ensemble averages of each experiment (e) (**p<0.01, ***p<0.001 compared to WT; one-way ANOVA with Bonferroni post-hoc test (c) or Welch ANOVA with Tamhane T2 test (d,e); n = 7 to 35 (given in parenthesis in each column); see Suppl. Fig. 5, 6 and Table 5 for more details).

Fig. 4 | Ectopic α-actinin-1 expression increases $Ca_V1.2$ open probability.

HEK293 cells were transfected with $\alpha_1$1.2, $\alpha_2\delta$-1, and β_{2A} plus, if indicated, α-actinin-1 before cell attached patch recording.

a, Representative single $Ca_V1.2$ channel recordings of WT $Ca_V1.2$ alone or with WT or E847K/E851K mutant α-actinin-1.

b, Mean assembly averages for all experiments for each combination.

c-e, Means ± SEM for availability (c), Po (d), and the mean of the current of a single channel calculated from the ensemble averages of each experiment (e) (*p<0.05, **p<0.01, ***p<0.001; unpaired t-test; n = 13 to 35; see Suppl. Fig. 7 and Table 6 for more details).

Fig. 5 | α-Actinin-1 E847K/E851K rescues open probability for $Ca_V1.2$ K1647E.

HEK293 cells were transfected with $\alpha_1$1.2 with the K1647E mutation, $\alpha_2\delta$-1, and β_{2A} plus α-actinin-1 WT or E847K/E851K before cell attached patch recording.

a, Representative single $Ca_V1.2$ channel recordings of $Ca_V1.2$ K1647E with WT or E847K/E851K α-actinin-1.

b, Mean assembly averages for all experiments for both combinations.

c-e, Means ± SEM for availability (c), Po (d), and mean of the current of a single channel calculated from the ensemble averages of each experiment (e) (**$p<0.01$; unpaired t-test; n = 16 to 35=0; see Suppl. Fig. 8 and Table 6 for more details).

Fig. 6 | Modulation of $Ca_V1.2$ surface expression via its interaction with α-actinin-1.

a, HEK293 cells were transfected with WT $\alpha_1$1.2, $\alpha_2\delta$-1, and β_{2A} ± WT α-actinin-1 and cultured for 22-24h before surface biotinylation. Shown are representative immunoblots of NeutrAvidin pull-down samples (from lysate containing 600 µg protein) and total lysate samples containing 20 µg protein. $\alpha_1$1.2 was detected with an antibody against its HA tag (*top*), which is present in all constructs used throughout this work. Pull-down and lysate samples are from the same blot but different exposures because signals from lysate samples were much stronger than from pull-down samples. Immunoblotting for vinculin (*middle*) and tubulin (*bottom*) indicated that comparable amounts of these intracellular control proteins were present in lysate samples. Their absence in pull-down samples as seen on the same blots showed that these prominent intracellular proteins did not undergo biotinylation as control for membrane integrity during surface biotinylation. Bar graph shows means ± SEM of the pull-down immunosignals in mutants relative to surface labelling of control $\alpha_1$1.2 samples lacking α-actinin-1 co-expression (mean set to 100%; see Methods; *$p<0.05$; two-tailed t-test; n = 7).

b, HEK293 cells were transfected with WT or K1647E mutant $\alpha_1$1.2, $\alpha_2\delta$-1, and $\beta_{2A,}$ and WT or E847K/E851K mutant α-actinin-1, or CFP alone as negative control and cultured for 22-24h before surface biotinylation. Shown are representative immunoblots of pull-down and lysate samples as in (a). Bar graph shows means ± SEM of the pull-down immunosignals in mutants relative to surface labelling in the WT/WT control (mean set to 100%; see Methods). **$p<0.01$, ***$p < 0.001$; one-way ANOVA with Tukey post hoc test; n = 4-5).

Fig. 7 | $Ca_V1.2$ mutations that affect α-actinin-1 impair gating charge movement and its coupling to channel opening.

HEK293 cells were transfected with $\alpha_1$1.2, $\alpha_2\delta$-1, and β_{2A} before whole cell patch recording in 20 mM Ba^{2+}.

a, Representative current traces of the first 2 ms obtained from recordings upon depolarizations from a holding potential of -80 mV to the indicated potentials (the voltage protocol is schematized in the upper left corner).

b, Representative current traces upon step depolarizations to the reversal potential (E_{rev}) for 20 ms to obtain movement of the ON-gating charges (Q_{on}), and subsequent to -50 mV for 10 ms to obtain tail currents (I_{tail}). Insets: magnifications of exemplary Q_{on} for $Ca_V1.2$ WT, K1647A, Y1649A, I1654A, F1658A and K1662E.

c, Plots of I_{tail} (in this panel corrected for variations in cell capacitance) versus total detectable charge transfer for Q_{on}. Slopes of regression curves are strongly reduced for $Ca_V1.2$ K1647A, Y1649A and I1654A versus WT (see Table 7 for more details).

d, Means ± SEM of Q_{on} (in this panel corrected for variations in cell capacitance; *$p<0.05$; **$p<0.01$; one-way ANOVA with Bonferroni post-hoc test; n = 13-18; see Suppl. Fig. 9 and Table 7 for more details).

e, The reduction in slope of the regression curve of combined population data for K1647A, Y1649A and I1654A versus WT indicates reduced coupling of I_{tail} with Q_{on} when α-actinin binding to the IQ motif is diminished.

SUPPLEMENTAL MATERIAL

α-Actinin-1 promotes activity of the L-type Ca^{2+} Channel Cav1.2

Matthew Turner[1$], David E. Anderson[1$], Madeline Nieves-Cintron[2$], Peter Bartels[2$], Andrea M. Coleman[1,2], Peter B. Henderson[2], Kwun Nok Mimi Man[2], Vladimir Yarov-Yarovoy[3], Donald M. Bers[2], Manuel F. Navedo[2], Mary C. Horne[2#], James B. Ames[1#], and Johannes W. Hell[2#]

[1]Department of Chemistry, [2]Department of Pharmacology, and [3]Department of Physiology and Membrane Biology, University of California, Davis, CA 95616, USA.

Supplemental Figure 1. Amino acid sequence alignment of the membrane proximal portion of the C-terminal tail of L-type Ca^{2+} channels.

Bold refers to reference sequence (rat $\alpha_1$1.2), turquoise to divergency in amino acid sequence, red to residues K1647 and Y1649, which are important for α-actinin binding only, green to I1654, which is important for both, α-actinin and apoCaM binding, and yellow to F1658 and K1662, which are important for apoCaM binding only. Amino acid sequences were derived from species according to the numerical labeling[1-13]. Data were extracted and compiled from uswest.ensembl.org.

Supplemental Figure 2. Mapping the $Ca_V1.2$ IQ binding site in α-actinin and apoCaM.

a, Overlay of ^{15}N-^{1}H HSQC spectra of ^{15}N-labeled α-actinin-1 CH1/CH2 domain (residues 19-192) by itself (black peaks) and after addition of saturating, unlabeled IQ peptide (red peaks).

b, Overlay of ^{15}N-^{1}H HSQC spectra of ^{15}N-labeled α-actinin-1 EF-hand domain (residues 750-892) by itself (black peaks) and after addition of saturating, unlabeled IQ peptide (red peaks).

c, Overlay of ^{15}N-^{1}H HSQC spectra of ^{15}N-labeled α-actinin-1 C-lobe (α-actinin-1 EF34; residues 822-892) by itself (black peaks) and after addition of saturating, unlabeled IQ peptide (red peaks).

d, Overlay of ^{15}N-^{1}H HSQC spectra of ^{15}N-labeled apoCaM by itself (black peaks) and after addition of saturating, unlabeled IQ peptide (red peaks).

Supplemental Figure 3. NMR structural analysis using residual dipolar couplings (RDCs).

a,b, ^{15}N-^{1}H HSQC-IPAP spectra (Tjandra and Bax, 1997) of ^{15}N-labeled α-actinin-1_EF34 (A) or apoCaM (B) in the presence of saturating unlabeled IQ peptide. Representative and measured RDC values are marked above selected peaks. Samples used in HSQC-IPAP experiments were prepared by adding 5 mg of ^{15}N-labeled protein to 0.5 mL of NMR buffer containing 12 mg/mL of filamentous bacteriophage Pf1. HSQC-IPAP spectra were recorded in the presence of Pf1 (a,b) and absence of Pf1 (not shown). Residual dipolar couplings (RDCs) were measured (in Hz) as the difference in splitting for the ^{15}N-[^{1}H] doublet components relative to the isotropic $^{1}J_{NH}$ coupling. RDCs measured for 34 residues (α-actinin-1_EF34/IQ) and 36 residues (apoCaM/IQ) served as orientational structural restraints applied during the refinement phase of the structure calculation (Schwieters et al., 2003).

(C-D) Plots showing the correlation between observed versus calculated backbone RDCs predicted from the final NMR derived structures for α-actinin-1_EF34/IQ and apoCaM/IQ, respectively. The correlation coefficient (r^2) equals 0.99 and Q is 0.095 and 0.089 for α-actinin-1_EF34/IQ and apoCaM/IQ, respectively.

Supplemental Figure 4. Isothermal titration calorimetry of apoCaM added to IQ peptide.

a, Change of heat resulting from incremental addition of apoCaM (100 μM stock solution) into IQ peptide (10 μM) during ITC titration at 27°C in 50 mM HEPES (pH 7.4), 100 mM KCl, 0.05 mM EGTA and 1 mM $MgCl_2$.

b, A binding isotherm of apoCaM binding to IQ peptide was derived from the integrated heat at each injection after subtracting a blank titration (to remove heat of dilution). The binding isotherm for apoCaM binding to IQ exhibited no detectable heat signal above the noise level, consistent with low fractional binding under ITC conditions and/or low enthalpy caused by the relatively weak binding affinity (K_d = 10 μM, see Fig. 2e and Table 4).

c, Fluorescence polarization for binding of apoCaM (0.015 to 256 μM) to fluorescein-labeled WT IQ peptide (1.0 μM) in the presence of 100 mM KCl (black squares) versus zero KCl (red dots) at room temperature. The buffer was the same as in (a) except that KCl was excluded in the zero KCl sample. The data were fit to a one-site model (dotted lines) with K_d = 10 μM in the presence of 100 mM KCl and K_d = 2.6 μM in the absence of KCl.

Supplemental Figure 5. Representative single channel recordings and assembly averages for $Ca_V1.2$ WT, K1647A, F1648A, Y1649A, I1654A, F1658A, and K1662E.

HEK293 cells were transfected with $\alpha_1$1.2, $\alpha_2\delta$-1, and β_{2A} before cell attached patch recording. Holding potential (HP) was -80 mV and test potential (TP) 0 mV. Shown are 20 consecutive sweeps from representative experiments (top) and mean assembly averages for all experiments for $Ca_V1.2$ WT and each mutant.

a, $Ca_V1.2$ WT versus K1647A, F1648A, Y1649A

b, $Ca_V1.2$ WT versus I1654A, F1658A, and K1662E.

$Ca_V1.2$ WT in and K1647A are replicated from Fig. 3 a,b for comparison with the other $Ca_V1.2$ mutants.

Supplemental Figure 6. Effects of $Ca_V1.2$ IQ mutants on single channel properties.

HEK293 cells were transfected with $\alpha_1$1.2, $\alpha_2\delta$-1, and β_{2A} before cell attached patch recording. Shown are dot plots and means ± SEM (whiskers) for availability (a), NPo (b), Po (c), the mean of the currents calculated from the ensemble averages of each experiment (d), and single channel conductances i (e) for $Ca_V1.2$ WT, K1647A, F1648A, Y1649A, I1654A, F1658A, and K1662E (**p<0.01, ***p<0.001 compared to WT; one-way ANOVA with Bonferroni post-hoc test (a) or Welch ANOVA with Tamhane T2 test (b-e).

Supplemental Figure 7. Effects of overexpression of α-actinin-1 on single channel properties of WT $Ca_V1.2$.

HEK293 cells were transfected with WT $\alpha_1$1.2, $\alpha_2\delta$-1, and β_{2A} plus, if indicated, α-actinin-1 WT or E847K/E851K before cell attached patch recording.

Shown are dot plots and means ± SEM (whiskers) for availability (a), NPo (b), Po (c), the mean of the currents calculated from the ensemble averages of each experiment (d), and single channel conductances i (e; *p<0.05, **p<0.01, ***p<0.001; unpaired t-test).

Supplemental Figure 8. α-Actinin-1 E847K/E851K rescues open probability for $Ca_V1.2$ K1647E.

HEK293 cells were transfected with K1647E $\alpha_1$1.2, $\alpha_2\delta$-1, and β_{2A} plus α-actinin-1 WT or E847K/E851K before cell attached patch recording.

Shown are dot plots and means ± SEM (whiskers) for availability (a), NPo (b), Po (c), the mean of the currents calculated from the ensemble averages of each experiment (d), and single channel conductances i (e; **p<0.01; unpaired t-test).

Supplemental Figure 9. $Ca_V1.2$ mutations that affect α-actinin-1 impair gating charge movement and its coupling to channel opening.

HEK293 cells were transfected with $\alpha_1$1.2, $\alpha_2\delta$-1, and β_{2A} before whole cell patch recording in 20 mM Ba^{2+}.

a, Dot plots and means ± SEM (whiskers) of Q_{on} determined at reversal potential (see Fig. 7 for details; *p<0.05; **p<0.01; one-way ANOVA with Bonferroni post-hoc test).

b, I-V curves. Currents were recorded upon depolarization from a holding potential of -80 mV to increasingly more positive potentials (insert on left). Shown are peak currents. Dashed lines indicate SEM. The WT Cav1.2 curve is reproduced in all graphs for the $Ca_V1.2$ mutants.

c, G-V curves. Tail currents (I_{Tail}) were recorded upon repolarization to -50 mV following depolarization from a holding potential of -80 mV to increasingly more positive potentials. Shown are fitted curves in tope panels and dot blots in bottom panels.

Supplemental Figure 10. IQ peptide binds with opposite polarity to α-actinin-1 versus apoCaM.

a, NMR structure of α-actinin-1 (cyan) bound to $Ca_V1.2$ IQ motif (red).

b, NMR structure of apoCaM (cyan) bound to $Ca_V1.2$ IQ motif (red).

c, NMR structure apoCaM (cyan) bound to the $Na_V1.2$ IQ motif (red). PDB accession number is 2KXW (Feldkamp et al., 2011). Non-conserved intermolecular contacts between hydrophobic side chain atoms are colored yellow. The β-methyl side chain atoms of $Na_V1.2$ residues A1909 and A1915 are 2.5Å away from side chain methyl atoms of apoCaM residues M109 and L85, respectively. The aromatic side chain atoms of $Na_V1.2$ residue Y1919 are 3.3 Å away from aromatic side chain atoms of apoCaM residue F141.

a-c, Black arrows depict directionality of the IQ helix.

d, Amino acid sequence alignment of IQ motifs from $Na_V1.2$, $Na_V1.5$, and $Ca_V1.2$. Residues that are conserved between Na_V and Ca_V are shown in boldface font. Lysine residues in $Ca_V1.2$ that form intermolecular salt bridges in the $Ca_V1.2$ IQ peptide complexes with α-actinin-1_EF3/4 and apoCaM and are not conserved between the Ca^{2+} and Na^{2+} channels are colored red.

Supplemental Figure 11. Structural modeling addressing the function of Y1649 in the $\alpha_1$1.2 IQ motif and how the E851K mutation of α-actinin affects its binding to the IQ motif

a, Y1649 stabilizes the α-helical conformation of the $\alpha_1$1.2 IQ motif and thereby α-actinin binding. Shown is a cartoon representation of $\alpha_1$1.2 IQ motif α-helix (orange) and α-actinin-1 EF3-EF4 (blue). Sidechains of key residues are depicted as stick representation and labeled. Y1649 is in close proximity to L1653, which is about one α-helical turn downstream of Y1649. Stabilization of this α helix ensures correct positioning of I1654, which is critical for binding to α-actinin. This figure was created using UCSF Chimera (Pettersen et al., 2004).

b-d, The lysine residue in the E851K mutation of α-actinin destabilizes the canonical EF hand structure. Conformers of the lysine residues when used to substitute E851 by itself or together with E847 in α-Actinin-1 and of the glutamate residue when used to substitute K1647 in the IQ motif were calculated for the structure of the complex between the IQ motif of $\alpha_1$1.2 and EF3_EF4 of α-Actinin-1 using the UCSF Chimera rotamer tool (Pettersen et al., 2004). The $\alpha_1$1.2 IQ α-helix is shown in orange and the α-actinin-1 EF3-EF4 in blue. Sidechains of key residues are depicted as stick representation and labeled. The lysine rotamers (thin sticks) are overlaid on top of the original E851 and E847 residues and the glutamate rotamers on top of the original K1647 residue.

b, Simulation of rotamers for the E851K mutation in α-actinin-1 to show possible conformations of the lysine sidechain.

c, Simulation of rotamers for the E851K mutation in α-actinin-1 and the K1647E mutation in $\alpha_1$1.2 to show possible conformations of the lysine and glutamate sidechains.

d, Simulation of rotamers for the E847K and E851K mutations in α-actinin-1 and the K1647E mutation in $\alpha_1$1.2 to show possible conformations of the lysine and glutamate sidechains.

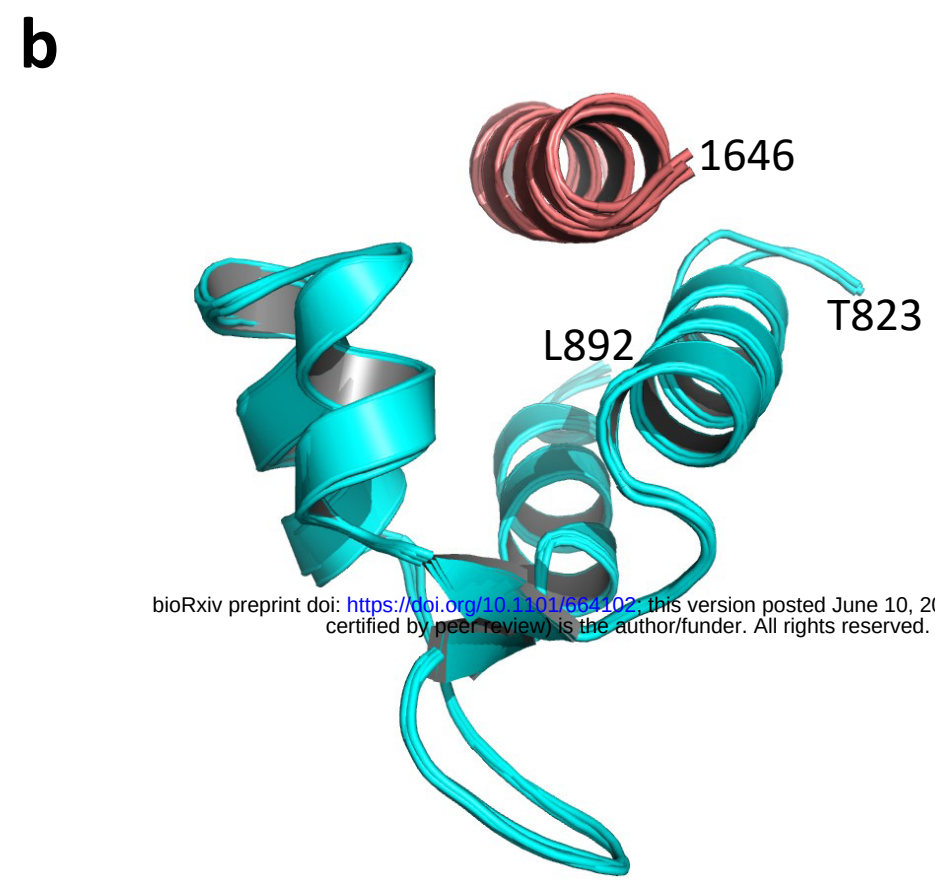

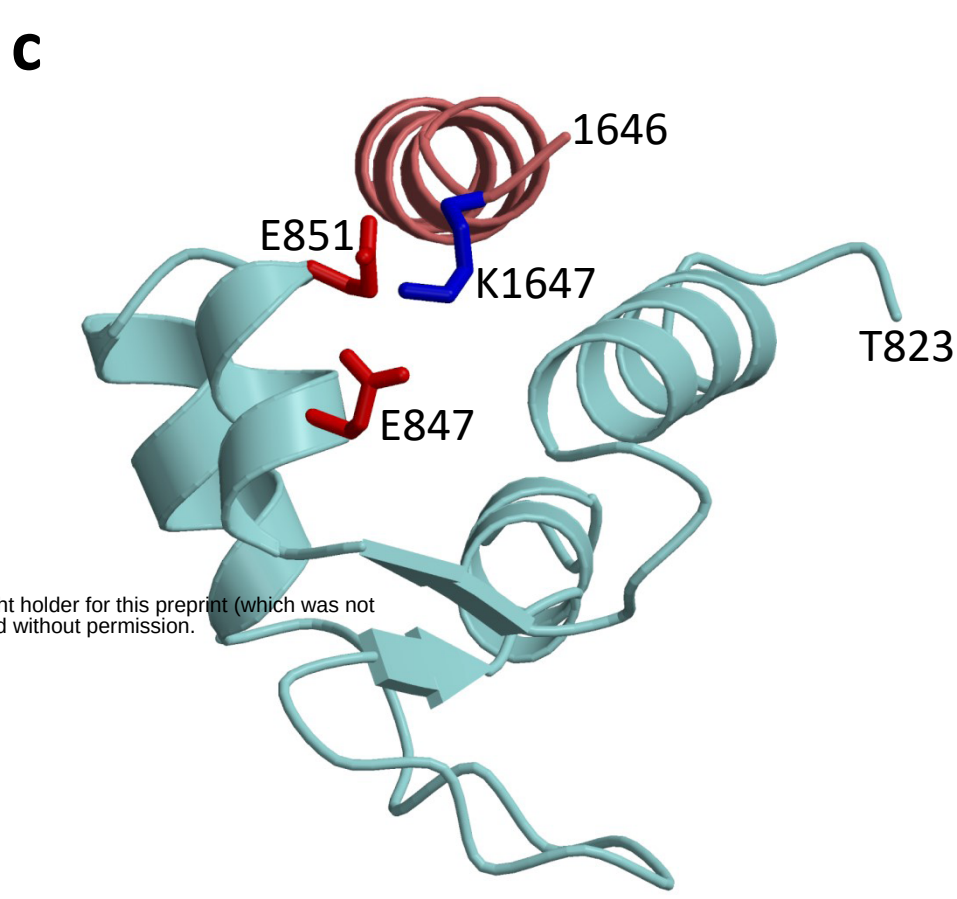

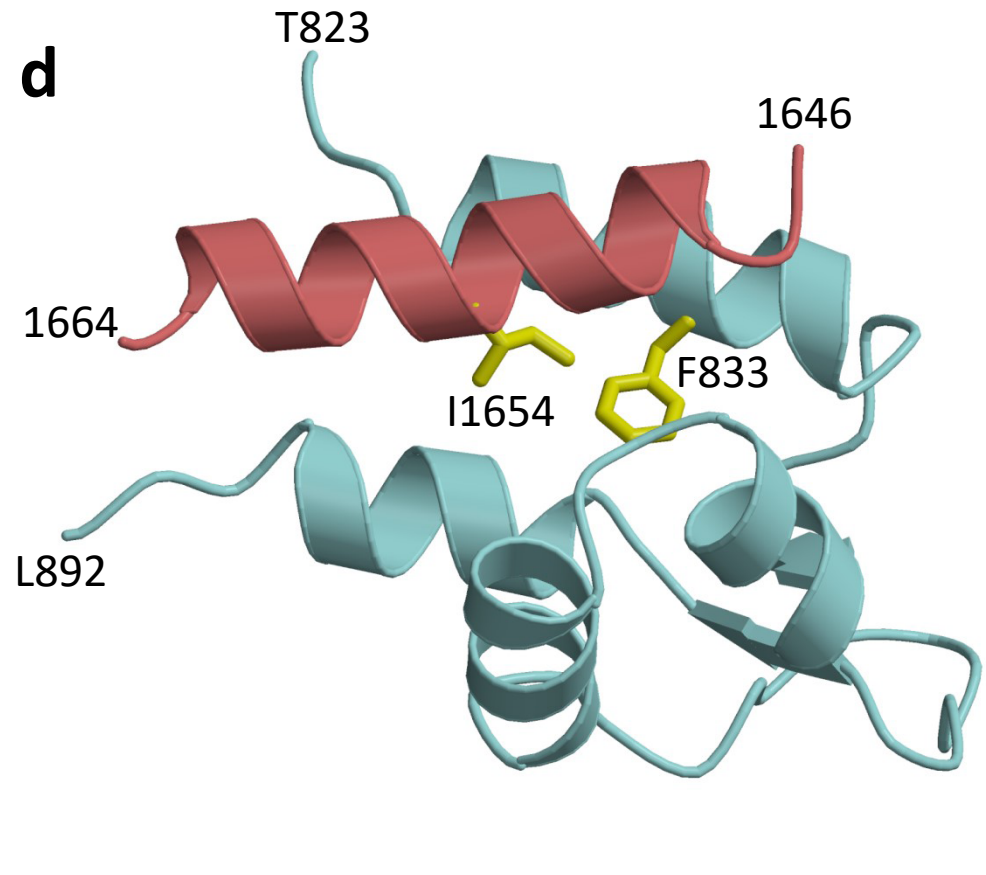

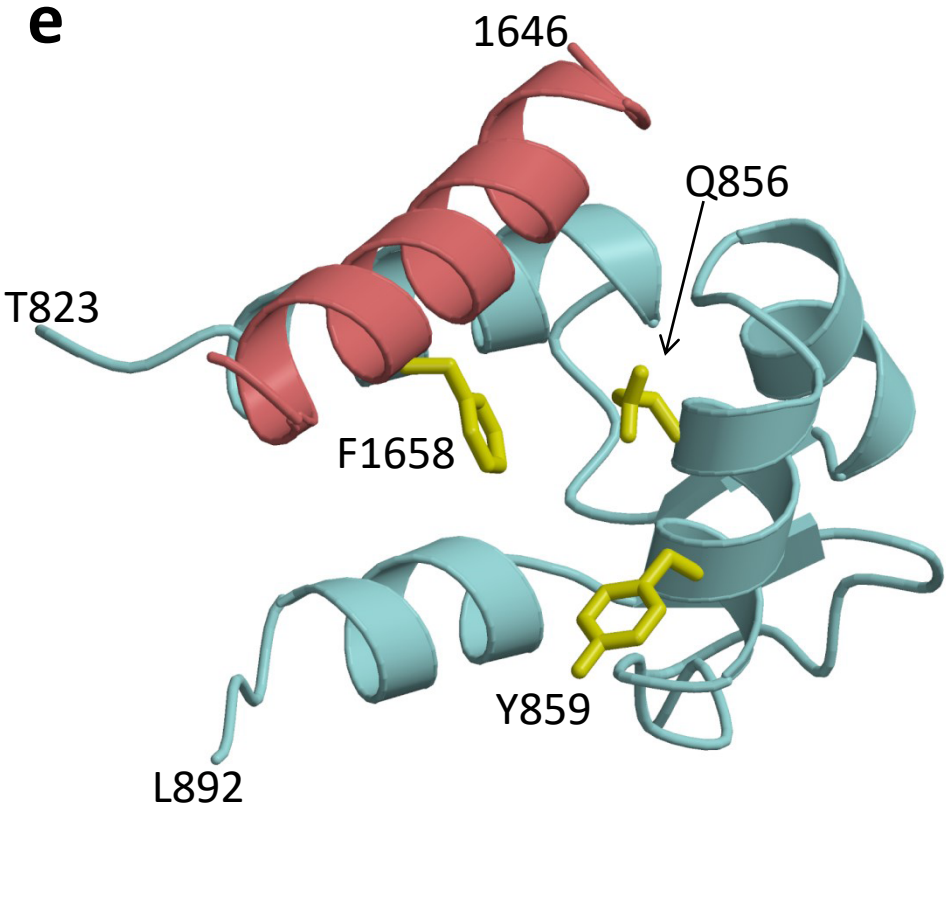

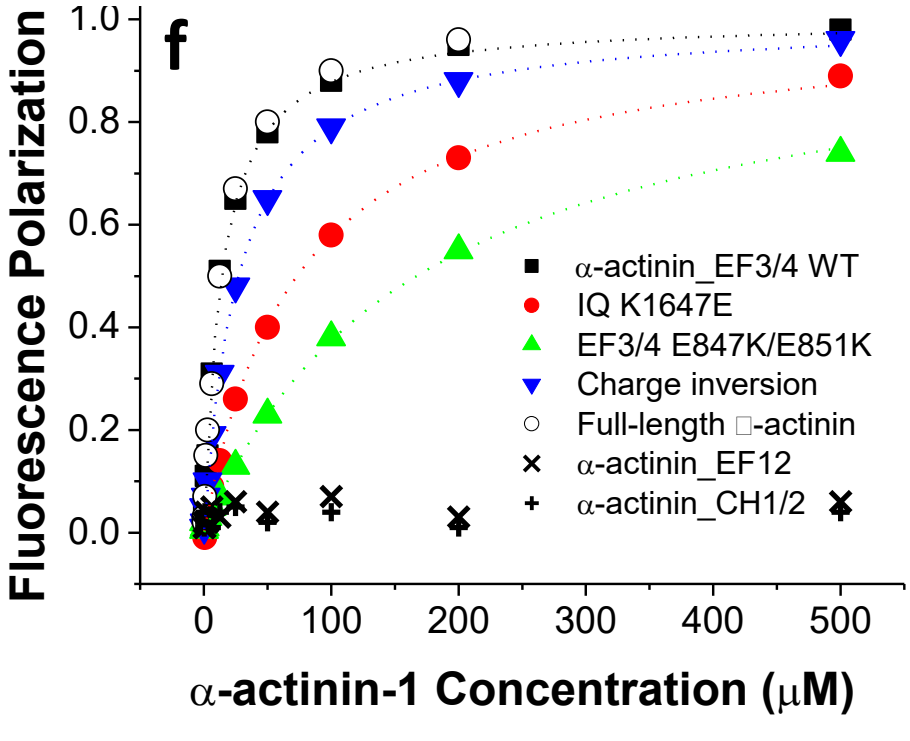

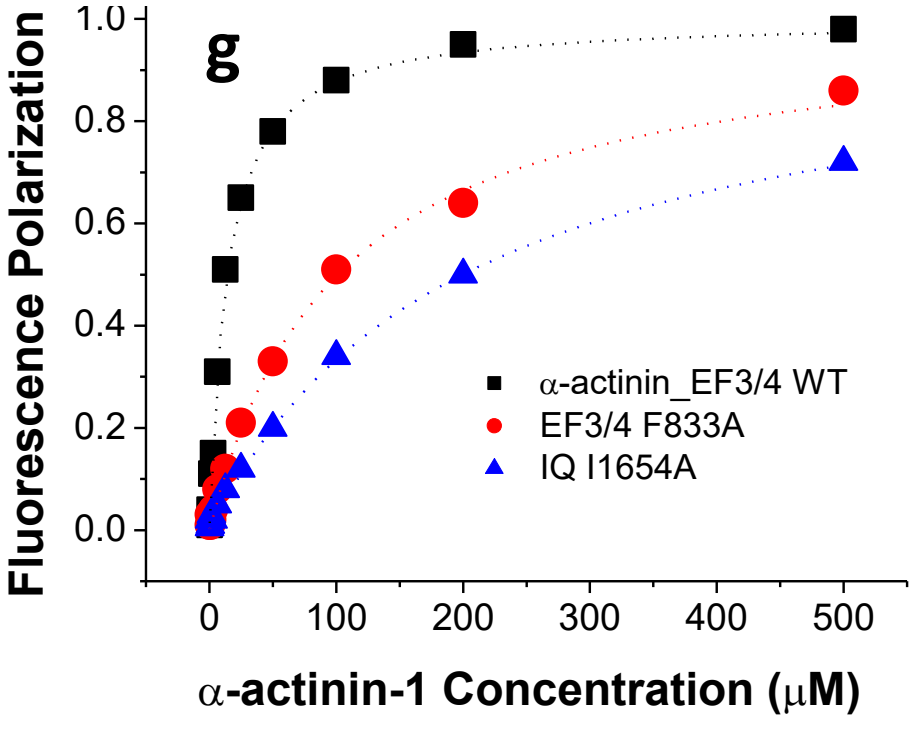

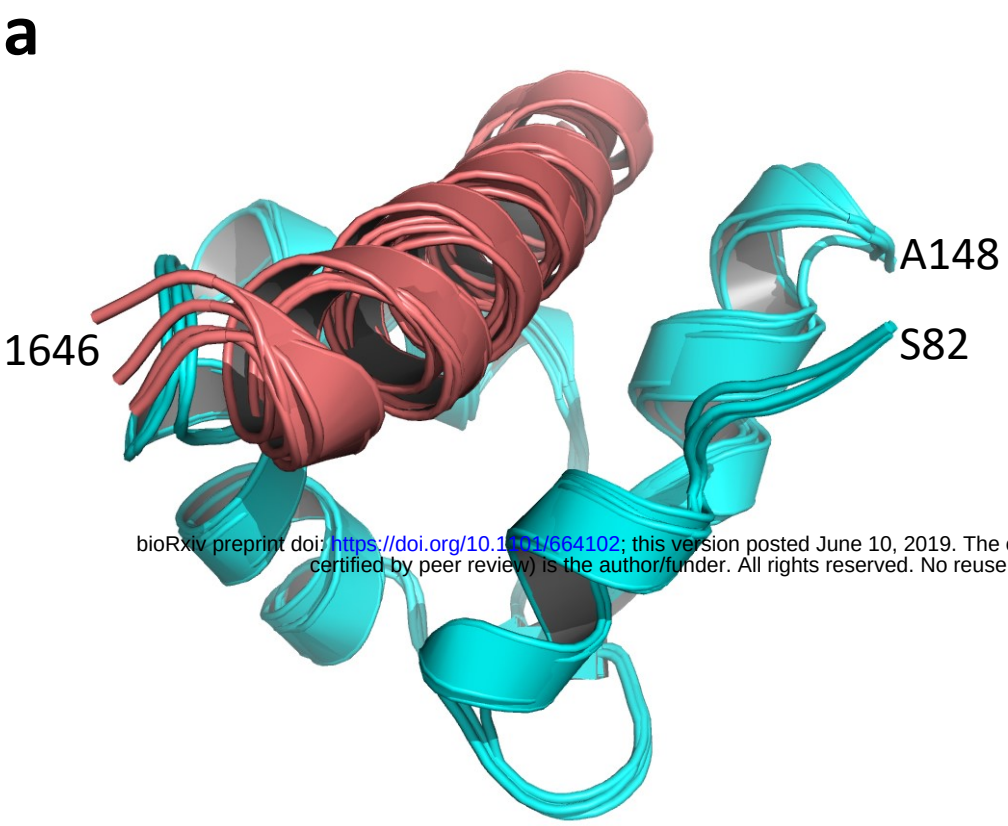

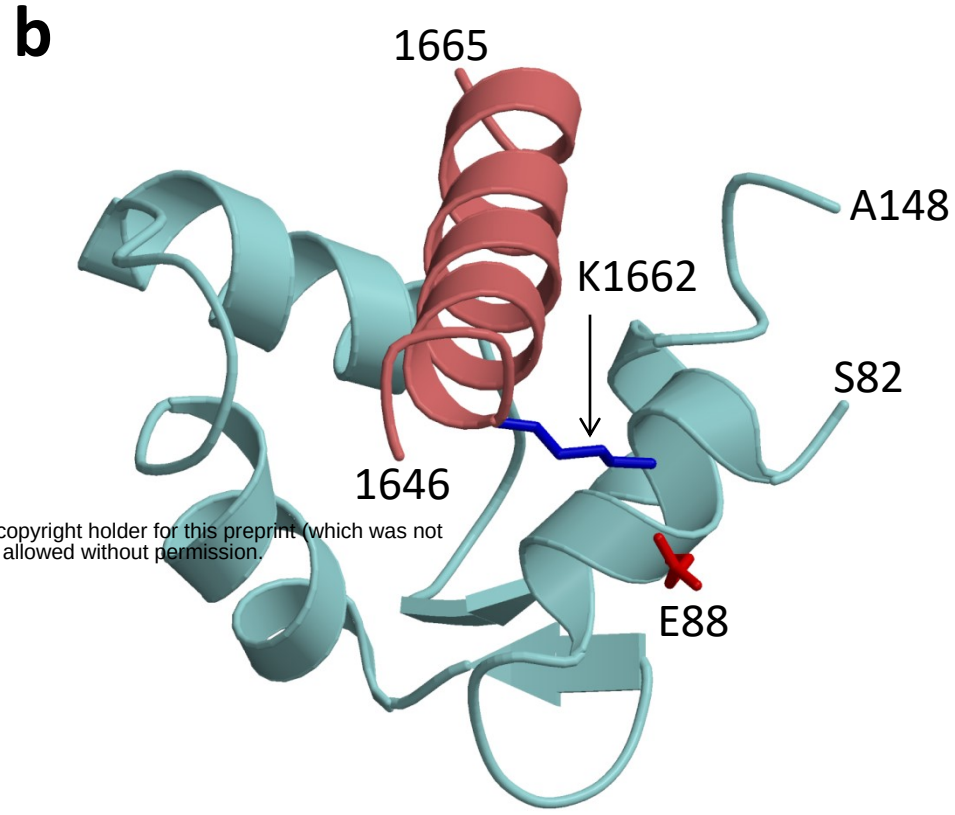

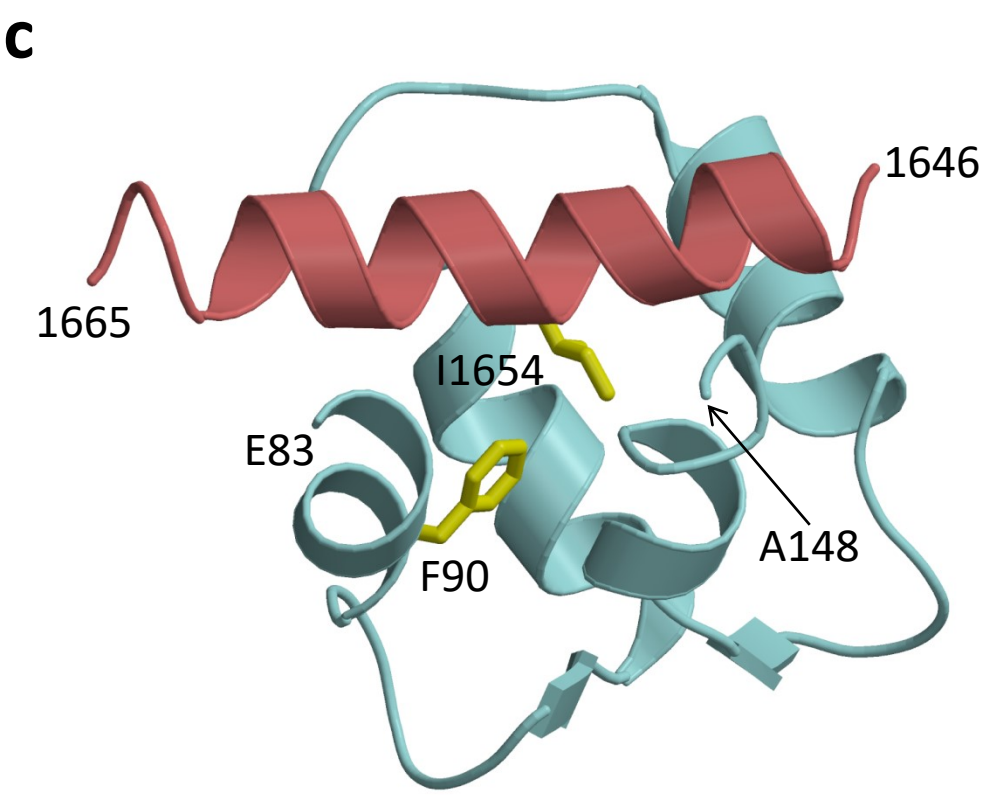

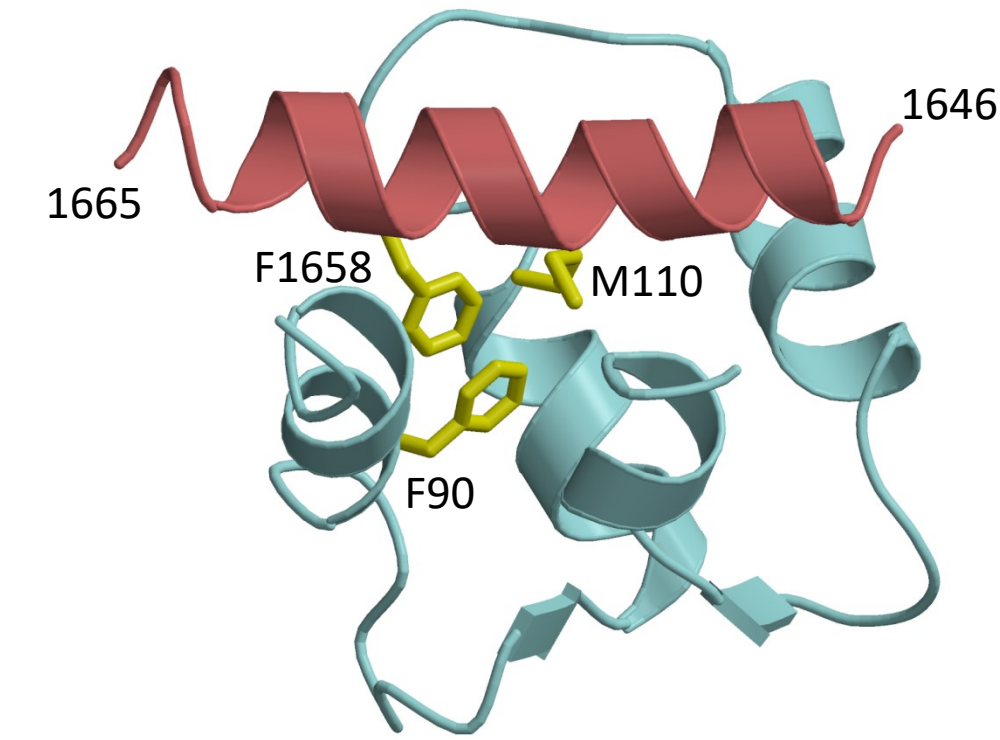

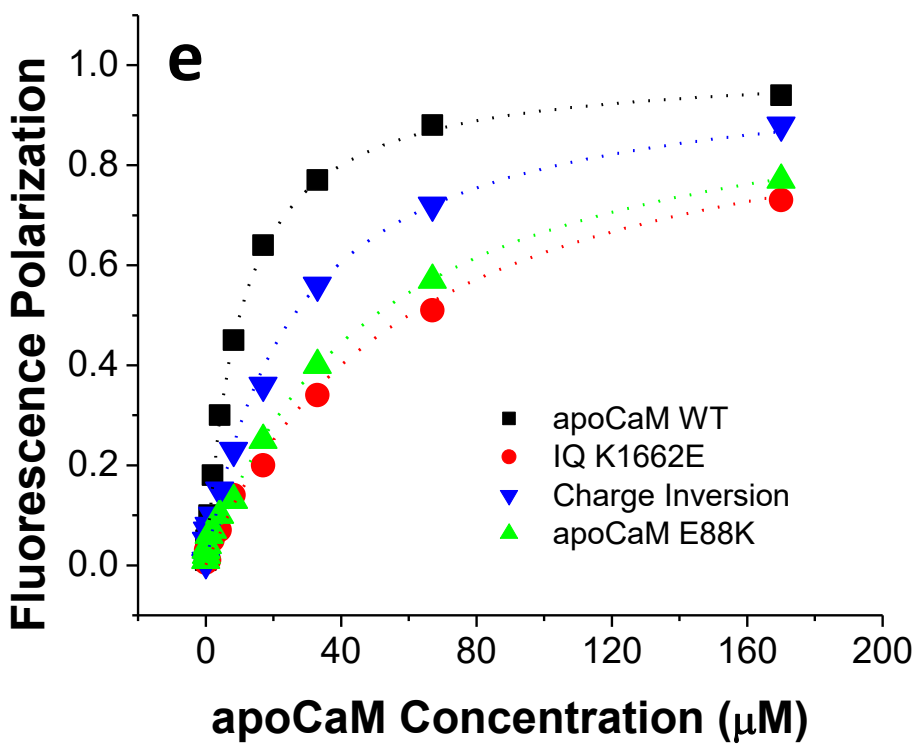

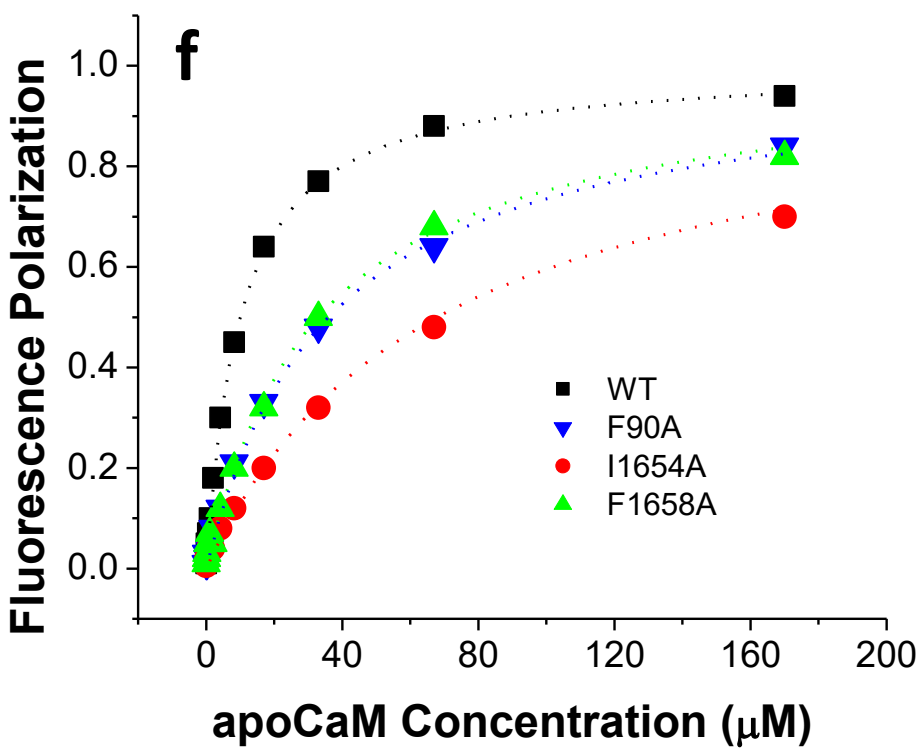

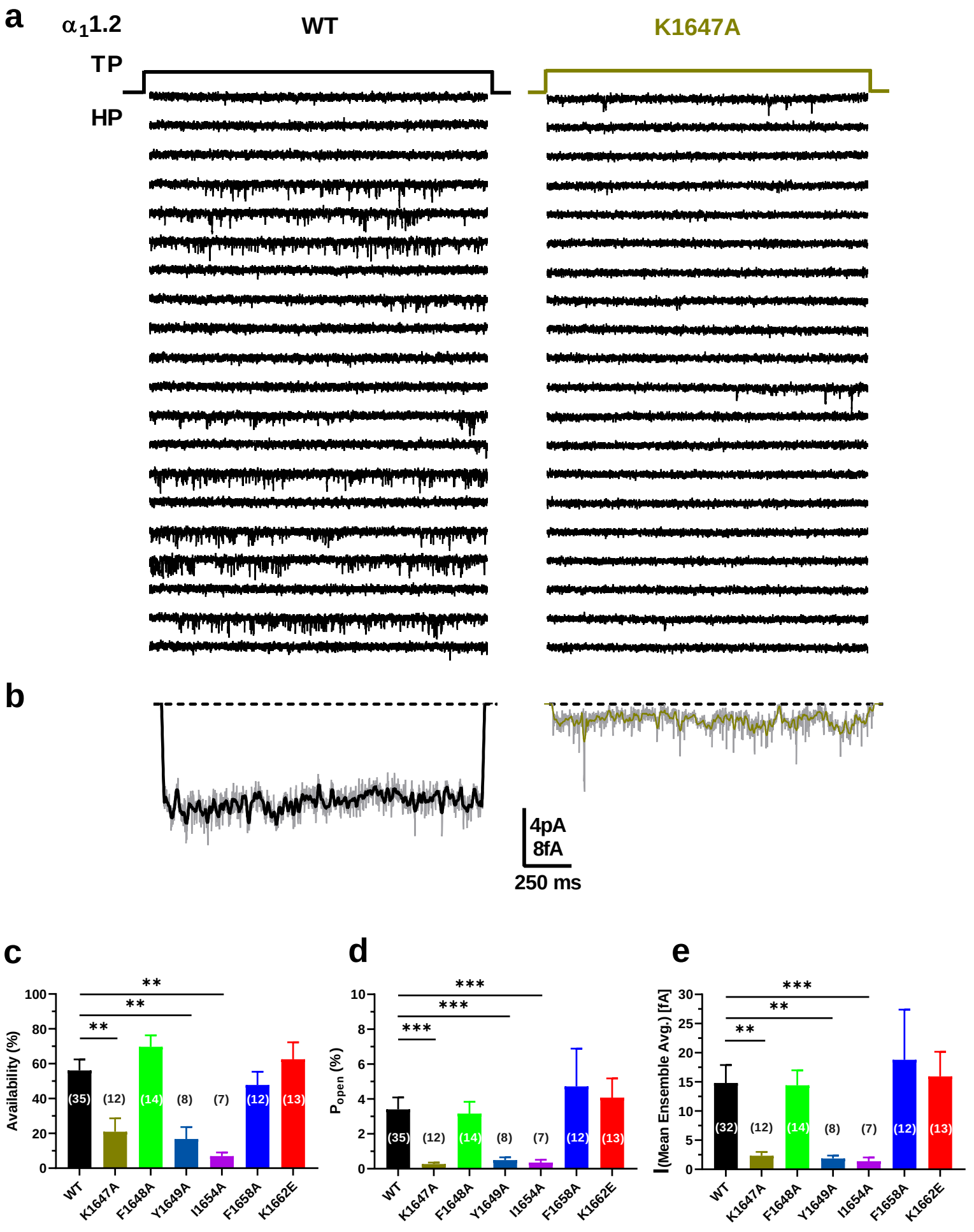
a
α1.2
WT
K1647A
TP
HP
b
4pA
8fA
250 ms
c
Availability (%)
d
Popen (%)
e
I(Mean Ensemble Avg.) [fA]
WT
K1647A
F1648A
Y1649A
I1654A
F1658A
K1662E
(35)
(12)
(14)
(8)
(7)
(12)
(13)
(32)
**
***

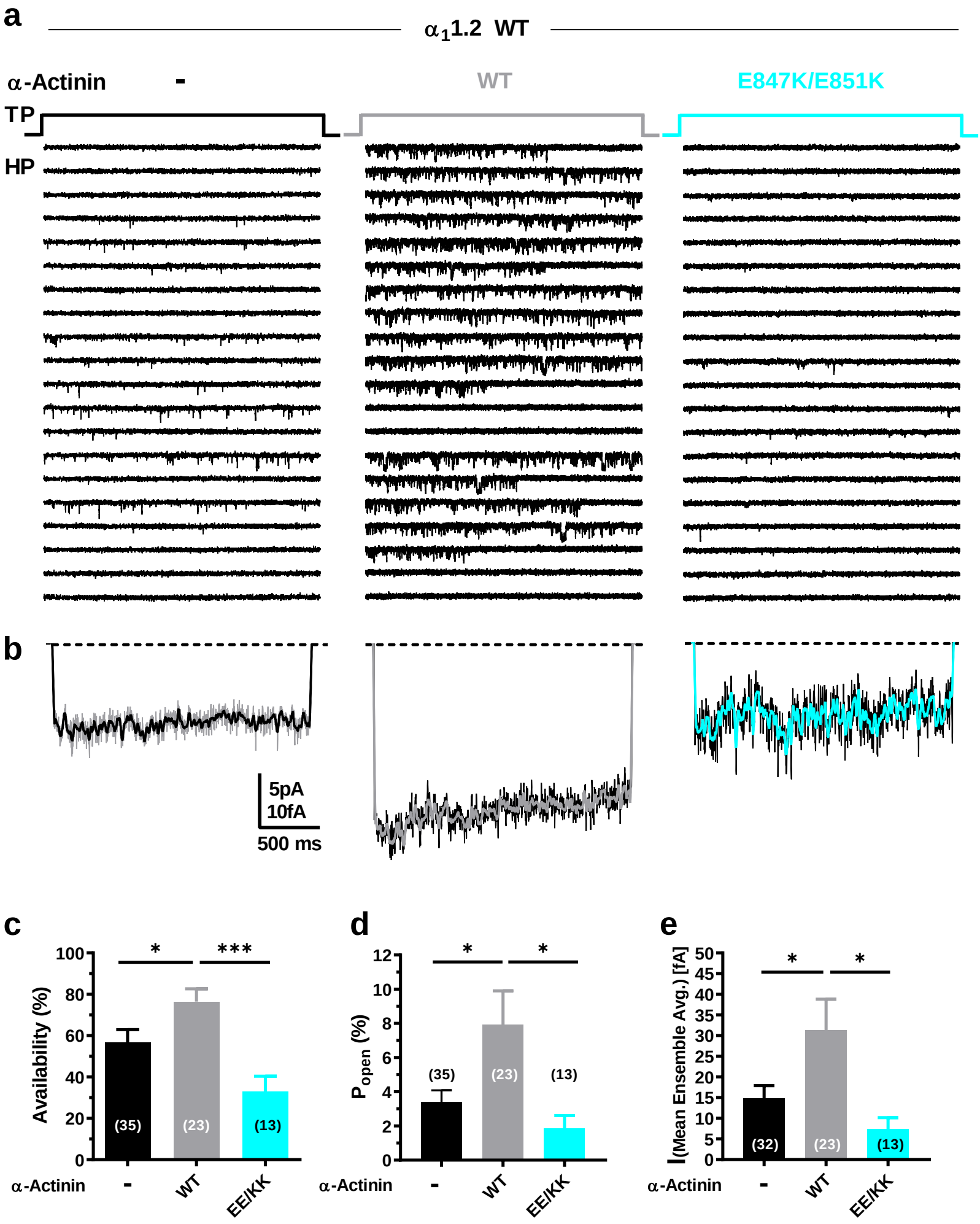

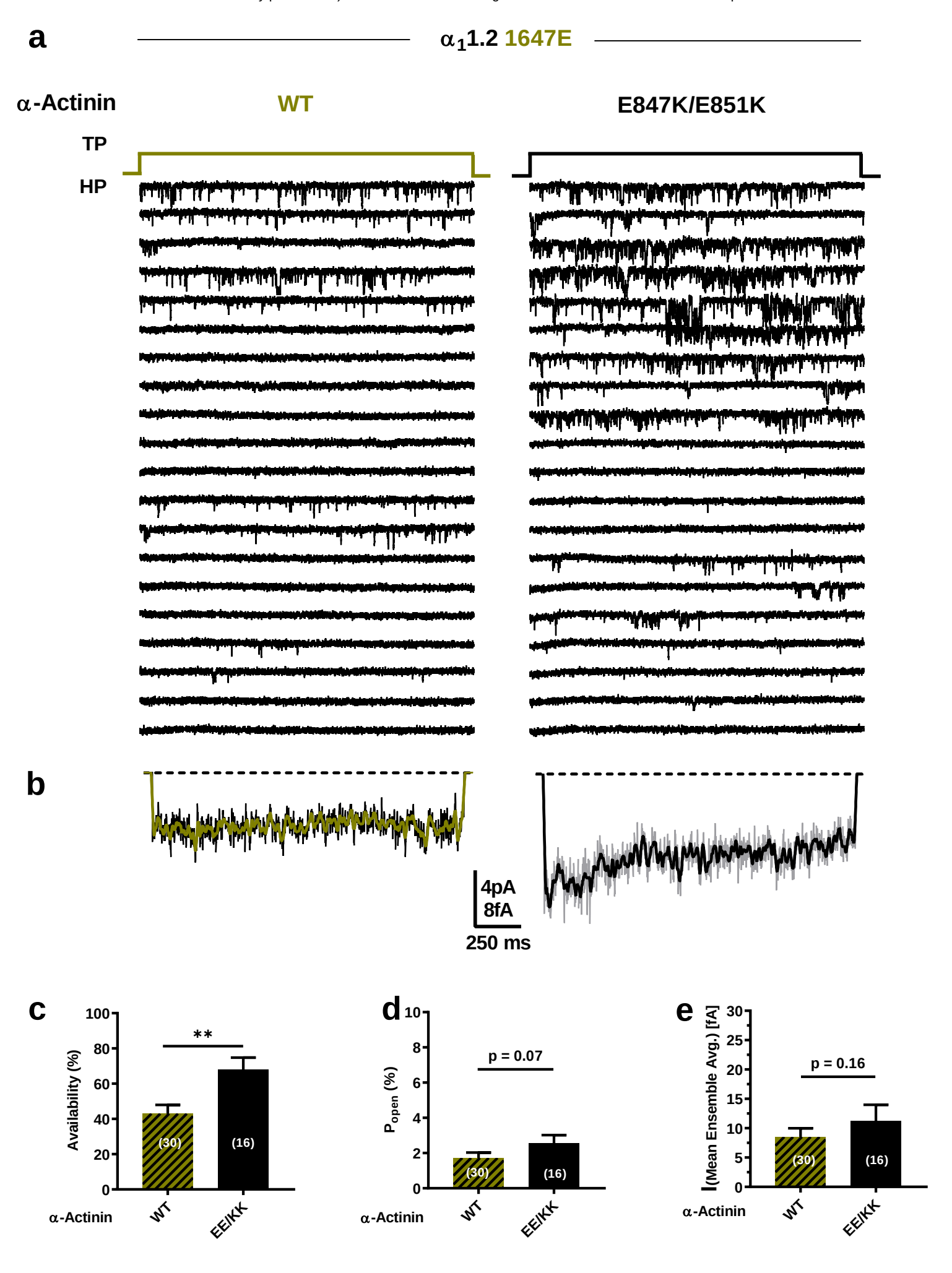
a
α1.2 1647E
α-Actinin
WT
E847K/E851K
TP
HP
b
4pA
8fA
250 ms
c
Availability (%)
100
80
60
40
20
0
**
(30)
(16)
α-Actinin
WT
EE/KK
d
Popen (%)
10
8
6
4
2
0
p = 0.07
(30)
(16)
α-Actinin
WT
EE/KK
e
I(Mean Ensemble Avg.) [fA]
30
25
20
15
10
5
0
p = 0.16
(30)
(16)
α-Actinin
WT
EE/KK

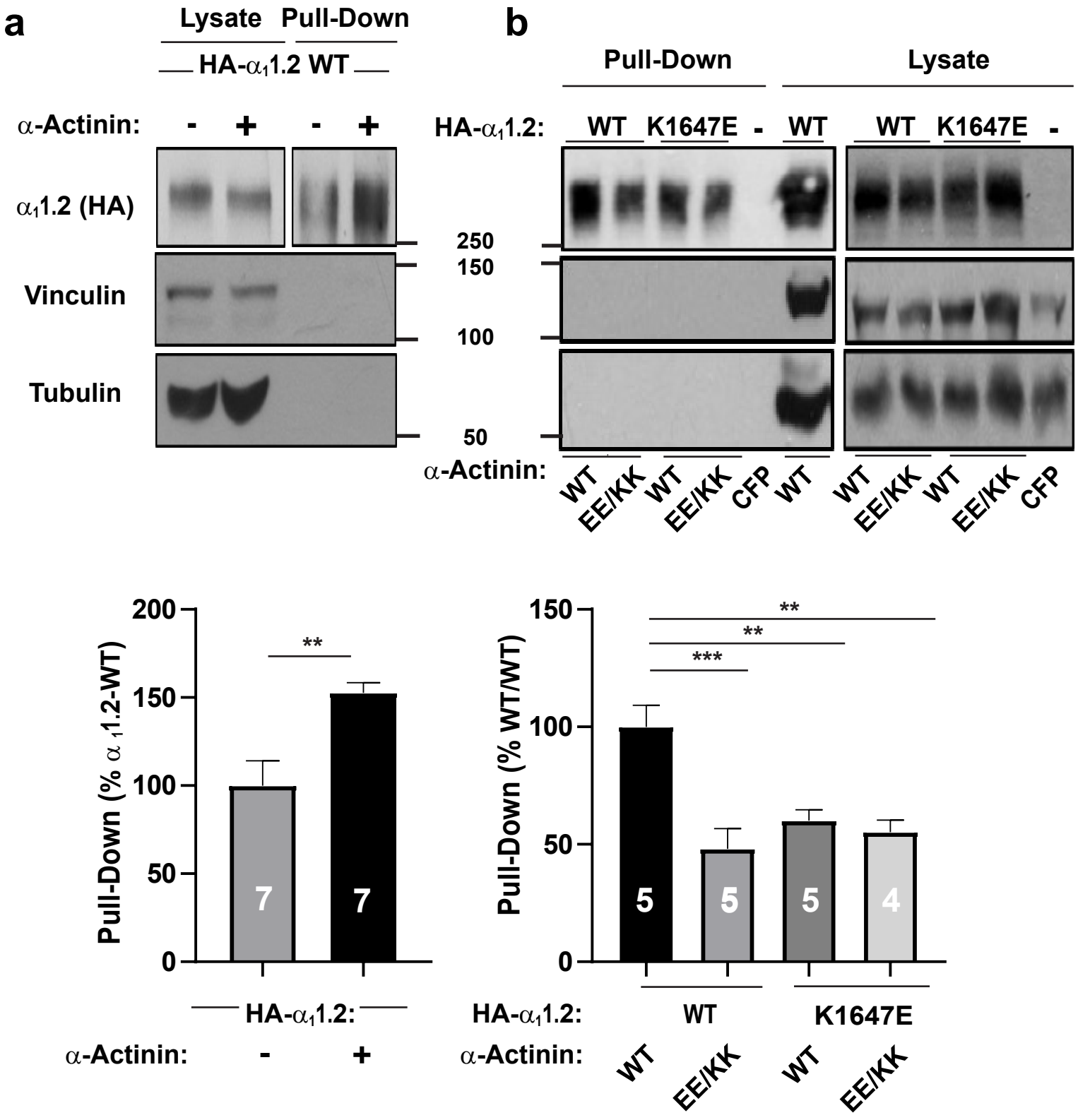

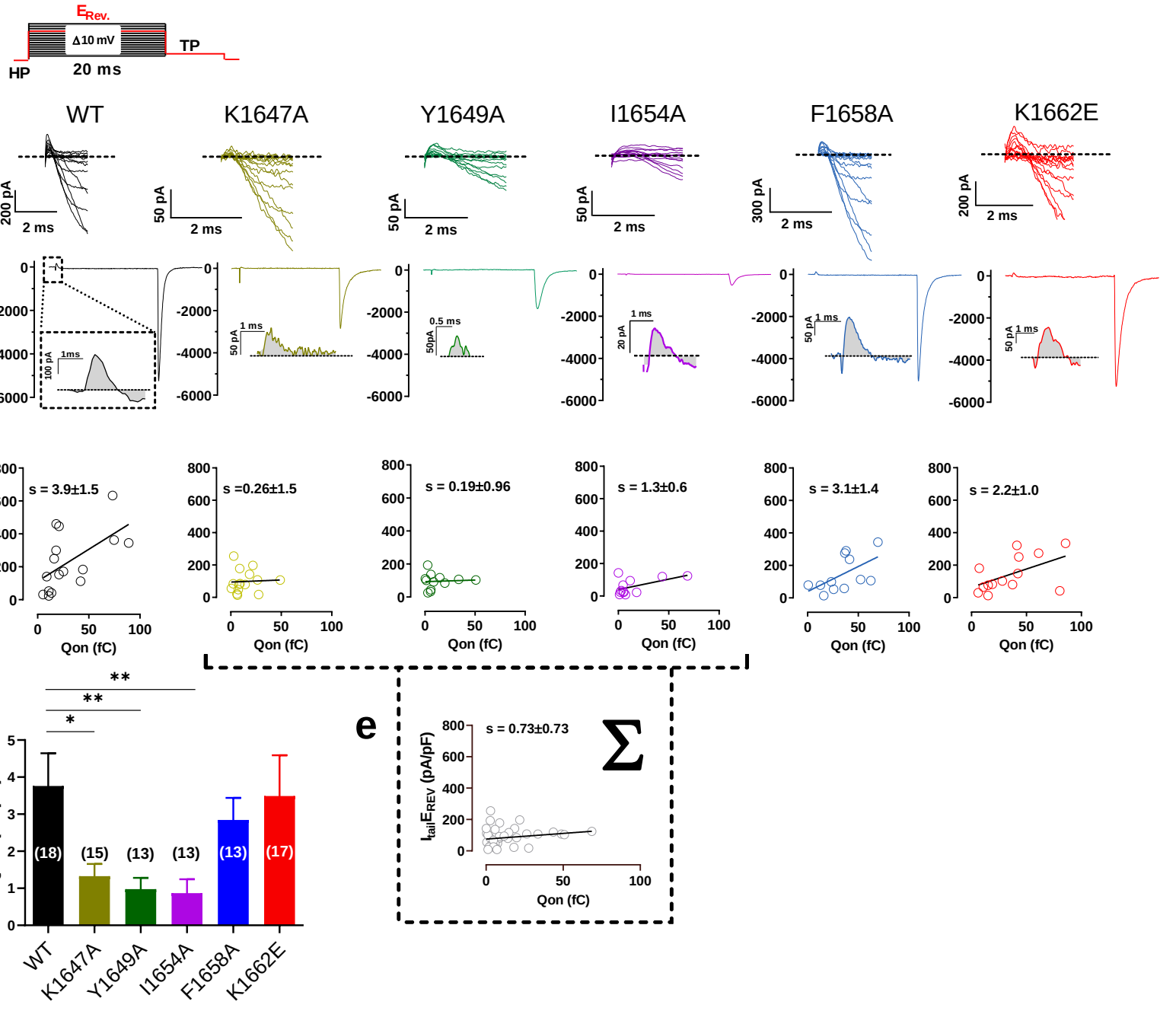
E_Rev.
Δ10 mV
TP
HP
20 ms
a
WT
K1647A
Y1649A
I1654A
F1658A
K1662E
200 pA
50 pA
300 pA
2 ms
b
Ba2+-current (pA)
0
-2000
-4000
-6000
1 ms
0.5 ms
100 pA
50pA
20 pA
c
ItailERev (pA/pF)
s = 3.9±1.5
s =0.26±1.5
s = 0.19±0.96
s = 1.3±0.6
s = 3.1±1.4
s = 2.2±1.0
Qon (fC)
d
Qon (fC/pF)
**
**
*
(18)
(15)
(13)
(13)
(13)
(17)
WT
K1647A
Y1649A
I1654A
F1658A
K1662E
e
s = 0.73±0.73
Σ